Research paper

A new strategy for the reinforcement of paraffin-based fuels based on cellular structures: The armored grain — Ballistic characterization

Riccardo Bisin, Christian Paravan [*]

Department of Aerospace Science and Technology, Politecnico di Milano, 34 via LaMasa, I-20156, Milan, Italy

ABSTRACT

Slow regression rate of the solid fuel is the main limitation for the use of hybrid rocket engines in high thrust applications. Paraffin-based fuels tackle this limitation thanks to the entrainment mass transfer. In this study, ballistic behaviors of conventional polymeric fuel (ABS) and paraffin-based blends are studied and compared with those of the *armored grains*. These latter are a new generation of fuels featuring 3D printed cellular structures embedded in the wax-based grain. The ballistic characterization focuses on the evaluation of the regression rate (r_f) and its dependence on the oxidizer mass flux. Relative ballistic grading of the formulations is pursued via thickness over time methods and an optical technique for r_f determination. The armored grains are reinforced by gyroid structures that are 3D printed using three different polymers (ABS, PLA, and Nylon 6) and two relative densities (10% and 15%). Despite the slow burning behavior of the printing polymers, the embedded reinforcement enhances the r_f of the paraffin-based formulations, with percent increases ranging from +48% to +91%. This result could be explained by the uneven and irregular texture of the burning surface promoting turbulence (and therefore, propellant mixing) and convective heat transfer. For both the armored grains and the paraffin-based formulations, blending the pristine paraffin wax with polymeric additives results in more viscous formulations and in a r_f reduction. Armored grain combustion performance makes this novel fuel an interesting candidate for high-thrust hybrid rockets.

1. Introduction

Hybrid rocket engines (HREs) are nowadays regarded as a promising propulsion solution for different aerospace applications spanning from access to space and space tourism to in-space navigation [1]. These systems feature simplicity, intrinsic safety (i.e., tolerance to fuel grain cracks), reduced recurring costs, throttling capability [2–4], and environmental friendliness if compared to solid rocket motors [5]. Yet, the use of HREs in high thrust applications is still hindered by the slow regression rate (r_f) of conventional polymeric fuels. High thrust performance in HREs are typically pursued by large regressing surface areas. These are achieved with the adoption of complex multiport geometries (such as triangular and quadrangular port configurations) [6]. However, with these solutions (i) the unburned fuel mass fraction is high, (ii) the design and fabrication of both the injection systems and the grain are complex, (iii) the volumetric fuel loading is lowered and (iv) the possibility of jeopardized grain structural integrity increases. In light of this, simple grain geometries (as the single, central port perforation) are more appealing in terms of applicability [1]. The solid fuel slow burning behavior, together with the low combustion efficiency hamper the hybrid rocket technology implementation in

operating systems. To cope with this problem, several strategies have been conceived: the exploitation of non-conventional grain geometries, the enhancement of the turbulence in the combustion chamber, and the use of liquefying fuels, such as paraffin waxes [5].

Oxidizer injection effects (standard and swirled flows) and turbulence generators have been studied to modify the HRE flow structure, with the aim of improving the (convective) heat transfer and, thus, the r_f and the combustion efficiency. The impact of the oxidizer flow distribution on the combustion performance of a hybrid rocket motor with standard axial injection was examined in Refs. [7,8]. Various injector patterns were experimentally and numerically analyzed by changing the diameter of injector holes and the distribution of the orifices in the injector plate. The findings of these researches stressed the importance of the oxidizer injection design for the development of HREs. Different types of injectors were considered by Bouziane et al. [9], who conducted a wide firing test campaign on the N2O/paraffin 1-kN hybrid rocket. The vortex injector provided the highest regression rate, followed by the hollow-cone and the showerhead. Swirl oxidizer injection was investigated by Yuasa et al. [10]. In this work, the average regression rate of swirled configurations increases up to 2.7 times with

---

* Corresponding author.
E-mail addresses: riccardo.bisin@polimi.it (R. Bisin), christian.paravan@polimi.it (C. Paravan).

Nomenclature

Acronyms and Abbreviations

ABS	Acrylonitrile Butadiene Styrene
CB	Carbon Black
DD	Diameter Difference (Regression Rate Data Reduction Technique)
FDM	Fused Deposition Modeling
HRE	Hybrid Rocket Engine
HTPB	Hydroxyl-Terminated PolyButadiene
MB	Mass-Based (Regression Rate Data Reduction Technique)
NY	Nylon 6
PLA	Polylactic Acid
SEBS-MA	Styrene-Ethylene-Butylene-Styrene copolymer grafted with Maleic Anhydride
SPLab	Space Propulsion Laboratory

Latin and Greek Symbols

$\bar{G}_{ox}$	Time- and space-averaged oxidizer mass flux, $kg/(m^2\ s)$
$\bar{p}_c$	Time-averaged combustion chamber pressure, MPa
Δt_b	Burning time, s
$\dot{m}_f$	Fuel mass flow rate, g/s
$\dot{m}_{ox}$	Oxidizer mass flow rate, g/s
ρ_f	Fuel density, g/cm^3
a_r	Pre-exponential factor in Eq. (1), $mm\ kg^{n_r}/[m^{2 \cdot n_r}\ s^{(1+n_r)}]$
D	Diameter, mm
G_{ox}	Oxidizer mass flux, $kg/(m^2\ s)$
m	Mass, g
n_r	Exponent in Eq. (1)
p_c	Combustion chamber pressure, MPa
r_f	Solid fuel regression rate, mm/s
t	Time, s

Fig. 1. Armored grain concept exploiting 3D printed gyroid reinforcement.

(i) pyrolysis/vaporization (as in conventional formulations), and (ii) instabilization of the melt layer formed at the fuel surface by the gaseous propellant stream. This instabilization provides an additional contribution to the r_f of liquefying fuels: values up to 3–4 times that of conventional polymeric formulations (e.g., hydroxyl-terminated polybutadiene, HTPB, and acrylonitrile butadiene styrene, ABS) are achieved [17].

Even though paraffin waxes are appealing fuels thanks to their high ballistic performance, the poor mechanical properties prevent their exploitation in large scale operating systems. Thus, the mechanical properties of paraffin fuels should be enhanced. This is generally pursued by blending the wax with polymers. On one hand, this improves the structural performance of the formulations. Yet, implementing this strategy increases the melt fuel viscosity reducing (or fully hindering) the entrainment mass transfer [18]. In this regard, several research groups are seeking the best compromise between fuel mechanical properties and r_f enhancement.

In this framework, the Space Propulsion Laboratory (SPLab) of Politecnico di Milano has proposed a new approach of reinforcing paraffin fuels exploiting 3D printing [19–23]. This new class of paraffin-based fuels is called *armored grains*. An armored grain consists of a 3D printed scaffold structure embedded in a paraffin-based matrix, as shown in Fig. 1. The 3D printed reinforcement provides mechanical support for the paraffin-based formulation while serving as an additional fuel component. The gyroid, a triply periodic minimal surface cellular structure [24], has been considered as the most suitable geometry for the 3D printed reinforcement [22].

In this study, the ballistic behavior of armored grains featuring different printing polymers for the gyroid and different formulations for the paraffin-based matrix are discussed and compared with traditional wax-based fuels and non-entraining formulations. This paper can be considered the companion Ref. [22], where the armored grain was presented and the pre-burning behavior and the structural assessment were addressed.

2. Background

Paraffin-based solid formulations are considered as an appealing opportunity for hybrid propulsion thanks to their fast regression rates. Interestingly, paraffin waxes are thermoplastic materials thus offering interesting features for manufacturing cost reduction [25]. On the other hand, paraffin waxes feature poor mechanical properties. Thus, the major challenge for the exploitation of their fast burning behavior is the development of formulations with a suitable combination of mechanical properties and ballistic responses.

2.1. Polymeric fuels vs. paraffin-based fuels: Ballistic and structural behavior

In HREs, the physical separation of the solid fuel and the oxidizer leads to a combustion process that is dominated by a diffusion flame

respect to the standard injection case. However, the swirling oxidizer flow created at the head-end diminishes its intensity along the length of the grain. This is particularly true for long motors with high length-to-diameter ratios [11]. As a result, the head-end region of the fuel regresses faster than the aft-end one. Researchers studied multi-location injections to counteract this swirl decaying and to provide swirling flow till the nozzle end [11]. This strategy was found to be effective in enhancing both the regression rate and the combustion efficiency. A hybrid engine featuring a coaxial, coswirling, counterflowing vortex combustion field in a cylindrical fuel port was conceived by Knuth et al. [12]. The engine exhibited regression rates up to seven times faster than those of standard injection central port perforated grains. A similar concept was employed in the vortex flow pancake (VFP) [13–15], which features a couple of fuel grains with a vortex injection between them. While effective in promoting fast r_f, and high combustion efficiencies (thanks to the oxidizer-fuel mixing induced by the vortex flow), the engine configurations discussed in Refs. [12–15] require exotic grain configurations that are best suited for relatively low thrust levels (e.g., in-space propulsion).

Paraffin-based fuels offer a low-cost and effective solution for the enhancement of r_f thanks to the entrainment mass transfer [16]. This phenomenon occurs in the so called *liquefying fuels*. Liquefying fuels feature mass transfer in the boundary layer by two mechanisms
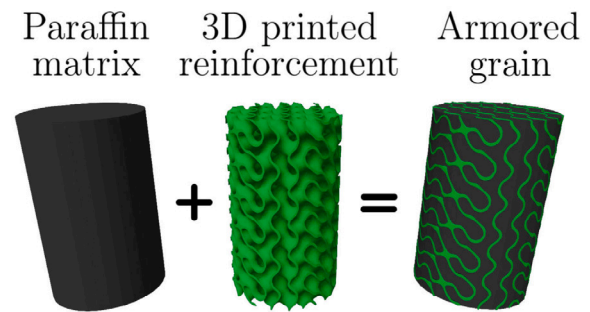
and driven by convection [5,26–29]. Analytical solutions and numerical models have been developed to describe the flame propagation above the fuel in the flow of an oxidizer [30–33]. The oxidizer flow over the fuel grain surface creates a turbulent boundary layer. Conventional fuels regress by pyrolysis/vaporization. Gasified fuel reacts with the oxidizer in the boundary layer providing the heat feedback to the grain and sustaining the combustion. Pyrolized/vaporized fuel mass blowing yields convective heat transfer blockage. As a consequence of this heat transfer reduction, and due to the limits for the fuel diffusion, fast r_f cannot be achieved. With conventional fuel formulations, r_f performance enhancement can be obtained by loading the fuel with metal particles. This strategy is discussed in detail in a comprehensive review by Risha [34], as well as in recent works considering nano-sized and mechanically activated metal fuels [35,36]. Metal fuel loading promotes enhanced r_f thanks to the augmented heat feedback toward the fuel grain by convection and radiation. A side effect of the metal addition is that particles leave the surface in the condensed phase, not contributing to the heat transfer blockage. Yet, the r_f increase by metal addition is relatively low when compared to the performance of liquefying fuel formulations. This latter class of fuels promotes fast r_f thanks to the entrainment mass transfer. In this mechanism (in turn due to a surface instability of the surface melt layer formed by liquefying formulations), convective heat transfer blockage has a reduced effect for a given r_f, since a significant fraction of the mass blown from the surface is in the condensed phase. While pyrolysis/vaporization is still present (and concur to limit the convective heat transfer, as in conventional fuels), the mechanical instabilization sprays fuel from the melted surface into the boundary layer. Low surface tension and low viscosity of the melted fuel favor the fuel entrainment [16,37]. Paraffin waxes are liquefying fuels offering relatively easy storage, handling and manufacturing.

The r_f is the main figure of merit of the ballistic performance and it is used to compare different fuels. The r_f is often reported as a function of the oxidizer mass flux G_{ox} according to:

$$r_f = a_r \cdot G_{ox}{}^{n_r} \tag{1}$$

with a_r being a constant depending on the fuel composition and the turbulence level and n_r with typical values ranging from 0.6 to 0.8. In alternate formulations, Eq. (1), the propellant mass flux is considered instead.

Relevant ballistic results extracted from the open literature are summarized in Table 1, where the $r_f(G_{ox})$ from Eq. (1) is shown. Collected data refer to single, central perforated grains, and are commonly evaluated via thickness over time (TOT) methods. These measurements are not instantaneous but are time- and space-averaged [38]. An extensive review of open literature results for non-metallized and metallized HTPB-based formulations is reported in Refs. [5,34]. Thermoplastic polymers considered as candidates for HREs include: polymethyl methacrylate (PMMA) [39,40], acrylonitrile butadiene styrene (ABS) [41–43], and several 3D printed grains including acrylonitrile styrene acrylate (ASA), polylactic acid (PLA), polypropylene (PP), polyethylene terephthalate glycol (PETG), and nylon [44]. Despite the use of different materials, all the studies highlight the slow burning behavior of polymeric fuels, especially if compared with paraffin-based formulations [16].

The r_f of the paraffin-based the SP1 A fuel (melting temperature of 69 °C) were measured by Karabeyoglu et al. [17] at two different scales. Fuel grains featuring 6.1 cm and 19.1 cm external diameters were fired at Stanford University and at NASA Ames Research Center, respectively. The study revealed that scale effect, length and pressure did not influence significantly the r_f, which was found to be G_{ox}-dependent through an exponent of 0.62. The r_f of the paraffin fuel was approximately three times larger than the one of HTPB. The test matrix was extended considering other paraffin fuel formulations [45]. The most promising ones were the paraffin waxes SP1 A and FR4045 (melting temperature of 61 °C), whose regression rates were approximately 5.5 and 5 times

the ones of the high density polyethylene (HDPE) baseline. The microcrystalline paraffin wax SasolWax 0907 was used as the solid fuel for a 200 N lab-scale HRE [46]. The regression rates and $r_f(G_{ox})$ power law approximation are reported in Table 1.

The fast r_f of paraffin fuels is achieved at the expense of poor mechanical properties, especially if compared to classical HTPB solid fuels and propellants. The latter are considered in this analysis because they feature a greater maturity and technology readiness level (TRL) than the solid fuels for hybrid propulsion. Table 2 summarizes typical tensile properties of HTPB-based solid propellants (taken as a suitable benchmark) and paraffin/paraffin-based fuels. The properties of HTPB formulations depend on several factors including the polymerization process, the molecular weight of the prepolymer, and the mass fraction and particle size/morphology of fuel (typically, Al) and oxidizer (ammonium perchlorate, AP) [49]. The elastic modulus of solid propellants ranges from 3 to 6 MPa depending on the formulation. The maximum tensile strength reaches 0.87 MPa, while the strain at maximum tension is around 27%. Higher values were measured by George et al. [47]: tensile strength of pure HTPB binder and HTPB-based propellants (HTPB+AP+Al) were found to be 1.87 MPa and 2.18 MPa, respectively. A 90% elongation was reached by both the HTPB binder and the HTPB-based propellants. Unlike HTPB, paraffin-based fuels exhibit a stiff and brittle behavior, as testified by the data reported in Table 2. DeSain conducted tensile tests on a paraffin wax with a melting temperature in the range 58–62 °C [50]. In this study, pure paraffin wax shows a similar maximum tensile strength as HTPB, but a much smaller percent elongation. On the contrary, the Young modulus (E) of paraffin wax is significantly higher than the one of HTPB. Tensile tests were conducted on the SasolWax 0907 micro-crystalline wax (congealing temperature in the range 83 to 94 °C) [51]. Results attest that the higher melting point of a paraffin wax the stronger its mechanical properties, in terms of E, strength and elongation at yield (σ_y and ϵ_y, respectively). Given the brittle behavior of paraffin wax, yield and break performance typically coincide. Moreover, the maximum elongation achieved by SasolWax 0907 does not exceed 1.1%.

The major concern when dealing with paraffin-based fuels is enhancing their mechanical properties without significantly reducing the ballistic behavior. The global research effort is focused on improving the strain energy of paraffin formulations trying to turn the brittle behavior into a ductile one. To do this, thermosetting and thermoplastic polymers are commonly blended with the pure paraffin waxes. Studies were conducted on HTPB-paraffin blends to exploit both the elasticity of the HTPB binder and the fast burning behavior of the paraffin wax [52–54]. Compression [52] and tensile [53] experiments showed that the addition of HTPB improved significantly the elastic properties (maximum deformation) at the expense of a drop of both E and maximum strength. The higher ductility and elasticity obtained by blending the paraffin wax with HTPB resulted in a slower ballistic response [52,54,55]. Several research groups explored different strengthening agents at different mass fractions and their impact on the mechanical, rheological and ballistic behaviors of paraffin fuels. Studies focused on polymethyl methacrylate (PMMA) [56], low density polyethylene (LDPE) [57], ethylene-vinyl acetate copolymer (EVA) [58, 59], styrene-ethylene-butylene-styrene grafted with maleic anhydride copolymer (SEBS-MA) [60,61], stearic acid (SA) [62]. All the aforementioned researches showed that blending paraffin with polymers could enhance the mechanical properties and the elasticity of the fuel. However, the viscosity of the melt fuel layer would increase with the addition of polymeric additives, in turn leading to a drop of the ballistic performance. Correlations between viscosity and regression rate are available in open literature [15,60,62–64]. These data help in identifying trends for suitable reinforcing compromises, yet the blending strategy inherently affects the r_f.

Table 1

Data from regression rate tests under gaseous oxygen: $r_f(G_{ox})$ for polymeric fuels and paraffin formulations. Single-port, center-perforated fuel grain configuration.

Fuel	$r_f(G_{ox})$, [Eq. (1)]		Oxidizer mass flux range,	Notes	
	$a_r\ \left[\frac{(mm/s)}{(kg/(m^2\ s))^{n_r}}\right]$	n_r	G_{ox} [kg/(m^2 s)]	Grain length × initial port diam. [mm]	Ref.
HTPB	0.087	0.53	60–300	250 × 12	[47]
	0.044	0.66	175–320	457 × 64	[48]
ABS	0.127	0.37	80–160	60 × 5	[42]
	0.103	0.22	10–30	220 × 23	[43]
Paraffin, SP1A	0.117	0.62	15–370	775–1150 × 75–150	[17]
Paraffin, FR4550	0.081	0.73	43–119	170 × 14–24	[45]
Paraffin, SasolWax 0907	0.071	0.79	45–110	220 × 15–20	[46]

Table 2

Tensile properties of HTPB-based propellants and paraffin fuels.

Fuel	Young modulus,	Yield stress,	Yield strain,	Notes		
	E [MPa]	σ_y [MPa]	ϵ_y [%]	Pull rate, [mm/min]	Temperature, T [°C]	Ref.
HTPB-based propellant	5.3–6.0	0.75–0.87	23–27	5.9	20	[49]
Paraffin, Aldrich's wax[a]	199.5	0.94	0.53	5.8	n.a.	[50]
Paraffin, SasolWax 0907[a]	512	1.78 ± 0.07	1.05 ± 0.24	1	23	[51]

[a]For paraffin wax, the yield stress and the yield strain coincide with the tensile strength at break and the elongation at break, respectively.

2.2. 3D printing and the armored grain

In the recent years, the opportunities offered by the 3D printing have been seized in hybrid rocket technology [65]. The freedom of designing with reduced machining boundaries, the possibility of manufacturing complex structures and the availability of different polymeric materials fostered the use of 3D printing to produce solid fuels characterized by standard [41,44,66,67] or complex geometries [68–71].

Whitmore and co-workers [41,66] focused on ABS printing. This thermoplastic polymer revealed to be a convenient replacement for the conventional HTPB. Production of HTPB grains involves expensive processes, such as mixing, degassing, casting, and curing that are avoided when printing by fuse deposition modeling (FDM). A variety of 3D printed fuels was explored by McFarland and Antunes, who tested ABS, ASA, PLA, PP, PETG, nylon, and PLA with aluminum particles (PLA-AL) [44]. Additive manufacturing was also exploited to produce ABS grains with helical ports at various helical pitch ratios [69,70]. The helical port geometry modified the internal flow properties and boosted the r_f up to four times with respect to conventional straight port grains. According to the authors, such a result is obtained thanks to (i) an increase in the skin friction of the printed helical fuel port structures, and (ii) the centrifugal component in the flow field pushing the flame zone closer to the wall surface and augmenting the flame diffusion efficiency while reducing the wall blowing effects. Firing tests revealed that fuels with more aggressive helical ports offered the largest initial r_f. However, during the combustion the port cross section becomes more cylindrical and the helical effect vanishes with time.

Another application of 3D printing consists in printing structures to carry a higher performing fuel. The printed scaffold acts as a support for the actual fuel, that has higher ballistic performance, such as paraffin wax. This is the rationale behind the armored grain, whose embryo can be identified in the Ref. [72]. In this latter study, a poly-urethane foam (PUF) was used as a strengthening structure for the paraffin matrix. The PUF manufacturing and the control of the cell size were the main drawbacks of this strategy [72]. Paraffin fuels embedding porous 3D printed ABS structures [73] and acrylic honeycombs with straight and swept cells were investigated in Refs. [74,75]. In these investigations, relatively small paraffin-wax fractions (25 vol%) were used to impregnate FDM-printed domains. The use of suitable reinforcing structures was recently restarted at the Space Propulsion Laboratory (SPLab) of Politecnico di Milano [19,20,22]. The proposed solution consists of paraffin wax reinforced by 3D printed structures at different volume fractions. The gyroid was identified as the most promising reinforcement geometry in the light of its characteristics, as discussed in [22].

The first investigation involved the pre-burning characterization of the 3D printed gyroid reinforcement and of the armored grains [22]. Polylactic acid (PLA), acrylonitrile butadiene styrene (ABS), and nylon 6 (NY) were selected as the materials for the gyroid, whose volume fraction (infill) spanned from 7% to 15%. Good paraffin-polymers wetting and compatibility were attested by measuring the surface tension of the paraffin wax, the critical surface tension, and the surface free energy of the different polymers. Armored grains exhibited superior mechanical properties than the pristine paraffin fuel. The experimental results evidenced that: (i) armored grains exhibit a ductile behavior regardless the material used for the gyroid (PLA, ABS, NY); (ii) denser gyroids (higher volume fraction) led to better mechanical properties (deformation energy, higher compressive strength); (iii) the selection of the polymer for the gyroid influenced the mechanical properties and the trend of the stress–strain curve of both the gyroid itself and the armored grain.

The same idea of embedding gyroids in paraffin grain has been also exploited by Hill et al. [76,77], who focused on what was called the lattice-augmented paraffin fuel grains. The authors conducted combustion tests on a 2D optically accessible slab burner with gaseous oxygen, and on a hybrid rocket motor with nitrous oxide. First studies highlighted higher combustion efficiency but lower regression rate for the lattice-augmented fuels [76]. Another research revealed that the volume fraction of the gyroid affects the regression of the lattice-augmented paraffin fuel grains [77]. More specifically, a 5% volume fraction increased the r_f, while higher fractions showed an opposite effect. Other research groups conducted studies on paraffin-based fuels reinforced by nylon-12 scaffolds [78,79]. The initial goal was lowering the EVA content required for the structural performance of the grain by exploiting the benefit of an embedded nylon-reinforcement [78]. Firings of various reinforced wax helical grains were performed and r_f enhancements over straight-port equivalents were observed [79]. Paraffin-based fuels featuring inner ABS skeletons were considered by Bresler [43] and by Wang [80] with the aim of generating turbulence and improving both the r_f and the combustion efficiency. ABS structures with baffles were investigated in the former study, while nested helical structures were selected in the latter. Both the ABS-reinforced grains offered higher r_f values than the pure paraffin fuels.

3. Investigated fuels

The ballistic investigation discussed in this paper focused on the fuel formulations whose pre-burning and mechanical behaviors are discussed in Ref. [22]. These fuels can be classified in two groups:

Table 3
Investigated paraffin-based fuel blends.

Fuel	Mass fraction, [%]			Dynamic viscosity[a],	Density[b],
	SasolWax 0907	SEBS-MA	CB	η [Pa s]	ρ_f [kg/m³]
W1	99	0	1	0.0057 ± 0.0008	929
S05W1	94	5	1	0.0140 ± 0.0003	928
S10W1	89	10	1	0.0397 ± NAv.	928

[a]Plate-plate geometry, shear rate 1000 s⁻¹, T = 150 °C [15].
[b]Density is reported as theoretical maximum density.

paraffin formulations based on a micro-crystalline paraffin wax (Sasol-Wax 0907 [81]), and armored grains featuring 3D printed gyroid-like reinforcements. The ballistic performance of 3D printed ABS fuel grains were also evaluated to have a baseline of polymeric fuels not undergoing entrainment, but only pyrolysis/vaporization process. The samples feature single-central perforated-ports with 5 mm initial port diameter, 30 mm external diameter and 50 mm length.

3.1. Paraffin-based fuels

Both plain and blended paraffin-based fuels were considered. The starting paraffin is a microcrystalline wax (SasolWax 0907). The blends exploited 5 wt% and 10 wt% of styrene-ethylene-butylene-styrene grafted with maleic anhydride copolymer (SEBS-MA) [82] as reinforcing agent. All the tested paraffin-based fuels were loaded with 1 wt% carbon black (CB) and they are listed in Table 3. The thermal behaviors and the compressive properties of the fuel formulations are reported in [22]. Table 3 also shows the dynamic viscosity of the investigated formulations, whose values increase as the amount of SEBS-MA increases [15]. Such a viscosity enhancement is expected to reduce the entrainment ability of the fuel formulations [15,16,45,60, 62,63]. Paraffin blends were prepared by melt casting. Details on the manufacturing of solid fuel blends are reported in [60].

3.2. Armored grains

The investigated armored grains feature a gyroid lattice structure embedded in the paraffin-based matrix. The formulation of the latter was previously introduced (see W1, S05W1, and S10W1 in Table 3). All the tested grain configurations are listed in Table 4 and are named after the two main ingredients: the paraffin matrix (see Table 3) and the embedded gyroid structure. Concerning the inner gyroid reinforcements, three 3D printer filaments were used: polylactic acid (PLA) [83], acrylonitrile butadiene styrene (ABS) [84], nylon 6 (NY) [85]. The gyroids were printed by means of the commercial FDM 3D printer Prusa i3 MK3 [86] following the infill gyroid methodology reported in Ref. [22]. The gyroid pattern provided by the native slicer of the printer, the PrusaSlicer [87], is chosen and the infill density is set to 10% or 15%[1] (samples XX_YY_i10 and XX_YY_i15 in Table 4). The selected infill values were identified based on their mechanical properties enhancement [22]. As for the paraffin-based fuels, a melt casting procedure was exploited for the armored grains too: the 3D printed gyroid (PLA, ABS or NY at 10% or 15% infill) is produced and lodged in a cylindrical mold, where the melted paraffin wax (W1, S05W1 or S10W1) is poured. The casting temperature depends on the paraffin blend and spans from 90 °C to 120 °C for the W1 and S10W1, respectively.

The experimental test campaign on the armored grains of Table 4 inspects the influence of different features on the ballistic response. More specifically, the impact of the 3D printer polymer on the grain is addressed by using PLA, ABS and NY for the gyroids with 15% infill (W1_XX_i15 set in Table 4). The infill of the ABS gyroid was reduced

to 10% to increase the amount of paraffin inside the fuel grain, and to boost the r_f (W1_ABS_i15 and W1_ABS_i10 samples). In fact, the paraffin wax is the fast burning component of the armored grain rather than the polymer, being the r_f of the former significantly higher than the one of the latter [42,43]. Finally, the SEBS-MA blends (S05W1 and S10W1) were also used for the armored grains (XX_ABS_i10 set in Table 4) to evaluate the effect of the viscosity increase of the paraffin matrix on the ballistic performance. The ABS was preferred over PLA and NY, because ABS exhibits the highest heat deflection temperature (HDT)[2] and it is the most thermally stable material [22]. In fact, the manufacturing of armored grains based on the SEBS-MA blends involves the casting of the S05W1 and S10W1 at temperature above 100 °C, a value that could lead to the softening of the polymers used for the gyroids. The ABS is less prone to this phenomenon than PLA and NY, thanks to a HDT of 101 °C (at 1.8 MPa) [84], while PLA and NY feature a HDT of 55 °C (at 0.45 MPa) [83] and of ≈93 °C (at 1.8 MPa) [88] respectively.

4. Experimental setup and data reduction techniques

The ballistic characterization was performed on the SPLab lab-scale HRE sketched in Fig. 2. The main observable of interest was the r_f. The r_f was computed via three different thickness over time (TOT) approaches: geometry-based, mass-based, and optical-based. The engine (Fig. 2(b)) is made up of an injection head, a pre-combustion chamber lodging the pressure transducer and the ignition system, a combustion chamber hosting the fuel grain, a post-combustion chamber to promote the combustion completeness, and a water-cooled brass nozzle. In the experimental campaign two different nozzles of 4 and 5 mm-throat were considered (the largest throat section being used for the fastest fuels tested at the highest mass flow rates). The injector head accommodates a quartz window for recording the combustion with a high-speed camera. The sample head-end is visible during the test enabling the port diameter measurement from each of the recorded combustion frames (Section 4.2). The oxidizer is injected with SN_g = 3.3.

Combustion tests were performed in gaseous oxygen (GOX), whose mass flow rate ($\dot{m}_{ox}$) was regulated by a digital flowmeter. The oxidizer mass flow rate was kept constant at 5 g/s or 7.5 g/s for the whole test duration. The grain ignition was achieved by a pyrotechnic primer charge placed in the pre-combustion chamber. This was ignited by resistive Kanthal filament heated by Joule effect. A piezo-resistive pressure transducer tracked the pressure evolution during the firing. The collected pressure trace (acquisition frequency 3 kHz) is shown in Fig. 3 and it is used to retrieve the combustion duration $\Delta t_b = t_{end} - t_{in}$. In particular, t_{in} is chosen as the time at which the chamber pressure starts raising because of the ignition of the primer charge, whereas t_{end} is defined by the injection of a gaseous nitrogen purge to quench the flame and stop the combustion. The oxygen and the nitrogen feeding lines were commanded by two synchronized electrovalves enabling the simultaneous switch from oxygen to nitrogen. Being the oxidizer mass flux the most significant parameter affecting the r_f [17,26], the Δt_b was

---

[1] The infill, also called relative density, indicates the volume fraction of the 3D printed polymeric structure inside in the fuel grain.

[2] The heat deflection temperature gives an indication of how the material behaves when stressed at high temperatures.

Table 4
Investigated armored grains. Note: the compositions are expressed as percentage by volume (infill), which does not coincide exactly with the percentage by weight because of the different density of the paraffin fuels (W1, S05W1, S10W1) and the polymers for the gyroids (PLA, ABS, NY).

Fuel	Volume fraction, [%]						Density[a],
	Paraffin matrix			Gyroid reinforcement			ρ_f [kg/m^3]
	W1	S05W1	S10W1	PLA	Nylon	ABS	
W1_PLA_i15	85	–	–	15	–	–	961
W1_NY_i15	85	–	–	–	15	–	949
W1_ABS_i15	85	–	–	–	–	15	947
W1_ABS_i10	90	–	–	–	–	10	942
S05W1_ABS_i10	–	90	–	–	–	10	941
S10W1_ABS_i10	–	–	90	–	–	10	941

[a]Density is reported as theoretical maximum density.

(a) Schematics of the test bench [89].

(b) Detailed view of the HRE components. Sizes are expressed in *mm*.
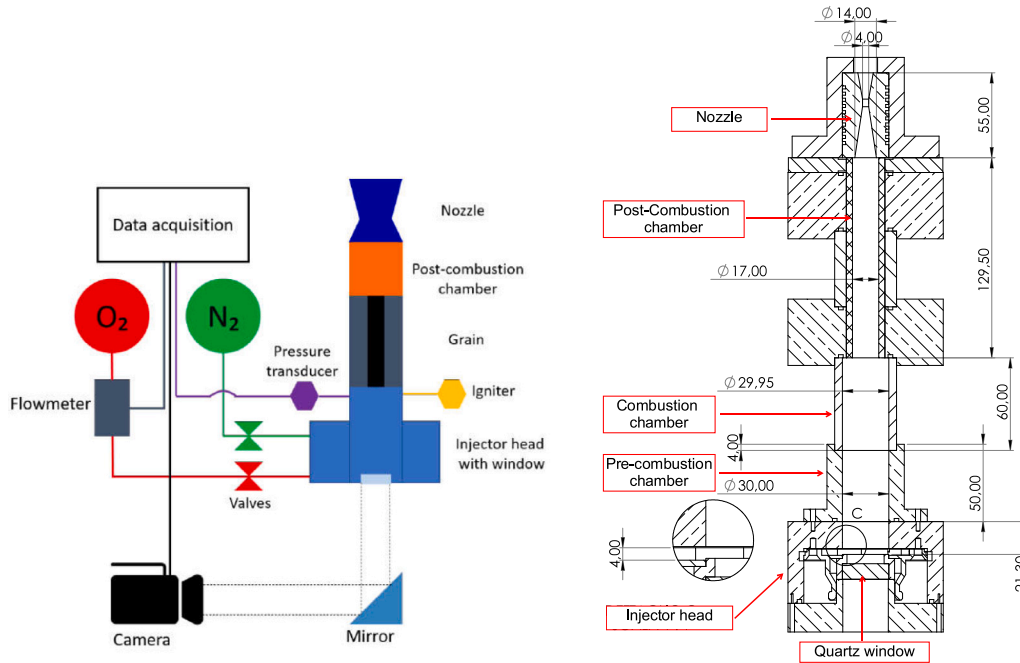
Fig. 2. SPLab lab-scale hybrid rocket engine.

tailored according to the fuel formulation in order to reach approximately the desired final diameter, thus the average G_{ox}. The burning time spanned from 4 s, for the fastest formulations (e.g. W1_ABS_i10), to 14 s, for the slowest ones (e.g. ABS).

4.1. Geometry-based and mass-based regression rate data reduction

Geometry-based (DD) and mass-based (MB) methods provide one single space- and time-averaged r_f for each firing. The two methods base the r_f evaluation on the variation of the port diameter occurred during the firing:

$$r_f = \frac{1}{\Delta t_b} \frac{D(t_{end}) - D(t_{in})}{2} \quad (2)$$

where $D(t_{in})$ is the initial port diameter (nominal value of 5 mm), whose actual value is measured by a caliper. The geometry-based and the mass-based techniques differ from each other on the $D(t_{end})$ determination. The geometry-based approach, also called diameter difference (DD) method [15], involves a direct measurement of the port diameter after the firing by means of a caliper. The port diameter is measured at the head-end and at the aft-end sections and the values are averaged.
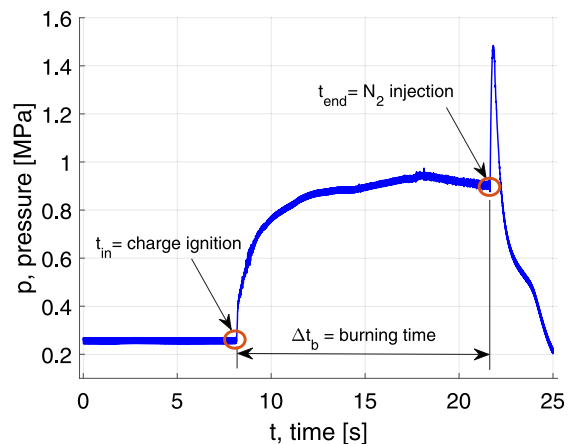

Fig. 3. Typical pressure trace of a combustion run (ABS fuel).

(a) Typical calibration frame, resolution: 1024x768 pixel^2.

(b) Typical extracted frame (S05W1 fuel). The red circle marks the burning surface.
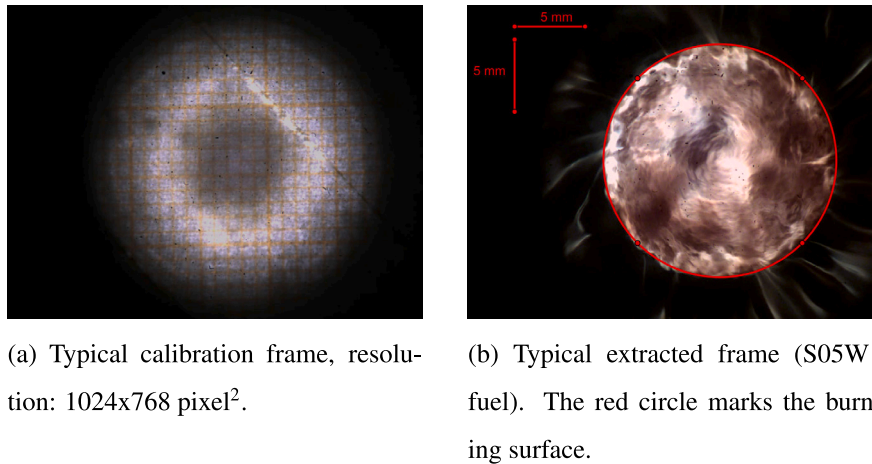
Fig. 4. Optical approach: (a) calibration phase, (b) image processing of the video recording the combustion of the fuel grain.

On the other hand, the mass-based (MB) approach evaluates the final diameter $D(t_{end})$ considering the fuel mass variation Δm_f before and after the combustion [17]:

$$D(t_{end}) = \sqrt{D(t_{in}) + \frac{4}{\pi} \frac{\Delta m_f}{\rho_f \cdot L_f}} \qquad (3)$$

where ρ_f and L_f are the density and the initial length (i.e., 50 mm) of the fuel grain, respectively. The theoretical maximum densities of the fuels in Tables 3 and 4 were used for ρ_f. For both methods, the average oxidizer mass flux ($\bar{G}_{ox}$) of the test was defined as the oxidizer mass flow rate ($\dot{m}_{ox}$ = 5 g/s or 7.5 g/s) divided by the average port area ($\bar{A}_b$):

$$\bar{G}_{ox} = \frac{\dot{m}_{ox}}{\bar{A}_b} = \frac{16 \cdot \dot{m}_{ox}}{\pi \cdot [D(t_{end}) + D(t_{in})]^2} \qquad (4)$$

Indeed, being the $D(t_{end})$ evaluated in two different ways (DD, MB), slightly different values are expected for the two methods. This leads to different r_f and $\bar{G}_{ox}$ values for the MB and DD techniques (see Eqs. (2) and (4)).

4.2. Optical approach

The optical-based method exploits the high speed video recording of the combustion. The SPLab lab-scale HRE in Fig. 2 enables a complete vision of the sample head-end during the firing by means of the quartz windows in the injection head. The solid fuel surface regresses in time and the port area enlargement is recorded by the Phantom V710 high-speed camera [89]. The video tracking the solid fuel regressing surface during burning is analyzed and the port diameters for selected frames are measured.

As shown in Fig. 2(a), the camera is positioned in front of the engine and the alignment between the camera, the reflective mirror and grain port grants the correct visualization of the central port. Before the test, a calibration video is recorded to convert distances measured in pixel to mm, see Fig. 4(a). The acquisition of the video recording starts once the oxidizer flow rate reaches the value set for the test conditions. After the recording starts, the ignition is triggered. All the operations are managed by a LabView routine implemented with a National Instrument Control Board. High-speed camera parameters (frame rate, shutter) were selected considering the expected regression rate and the brightness of the combustion process. The analyzed frames were extracted from the recorded videos, calibrated, and processed with the *Image Processing Toolbox* of MATLAB® [90]. For each extracted image, the intensity values and the contrast were adjusted via the *Imadjust* function [91], and the circular burning port area was manually marked by the operator and automatically measured by MATLAB via

the *Drawcircle* function [92]. A typical processed image is shown in Fig. 4(b). The extracted port diameter of the $i-$frame $D(t_i)$ was compared to the one from the previous frame $D(t_{i-1})$, and the corresponding regression rate and average oxidizer mass flux evaluated according to:

$$r_f(t_i) = \frac{1}{\Delta t} \frac{D(t_i) - D(t_{i-1})}{2} \qquad (5)$$

$$\bar{G}_{ox}(t_i) = \frac{\dot{m}_{ox}}{\bar{A}_{b,i}} = \frac{16 \cdot \dot{m}_{ox}}{\pi \cdot [D(t_i) + D(t_{i-1})]^2} \qquad (6)$$

The time interval Δt between the two consecutive $(i-1)$- and i-frames was retrieved considering the frame rate. The diameter sampling in time started from the frame in which the central port diameter was clearly visible (after primer charge ignition) and it was performed until the combustion end. Even though the videos were recorded at 400 fps (i.e. frequency of 400 Hz), the diameter sampling frequency for the $r_f(t_i)$ evaluation was reduced to 1 Hz (i.e. Δt = 1 s). In fact, sampling at higher values would have made the approach less robust and the r_f results less accurate. Higher sampling frequency means lower port diameter enlargement ($D(t_i) - D(t_{i-1})$ in Eq. (5)) and lower time interval Δt, in turn, a $r_f(t_i)$ highly sensitive to the manual diameter sampling by the operator.

The optical-based method can be considered a geometry-based method in which the sampling of the port diameters is performed multiple times during the firing via image processing, instead of using a caliper after the firing to measure an average r_f value (associated to an average $\bar{G}_{ox}$), that is assumed to be representative for the entire combustion process. This optical approach enables to identify a $r_f(G_{ox})$ correlation, since different discrete $r_f(t_i)$ and $\bar{G}_{ox}(t_i)$ values were evaluated during the firing.

5. Results and discussion

The results of the test campaign are summarized in Table 5, where the r_f were evaluated according to the geometry-based (DD) and the mass-based (MB) approaches. All the investigated fuels were tested at $\dot{m}_{ox}$ = 5 g/s. For the armored grain family featuring ABS gyroid with 10% infill (XX_ABS_i10 series) the $\dot{m}_{ox}$ was also increased to 7.5 g/s to inspect the effect on the r_f of higher $\bar{G}_{ox}$. The relative grading of the ballistic performance for the solid fuels is enabled by the similarity of the experimental conditions in terms of $\bar{G}_{ox}$ and $\bar{p}_c$. Figs. 5 and 6 show a paraffin fuel (W1) and an armored grain (W1_PLA_i15) before and after the firing.
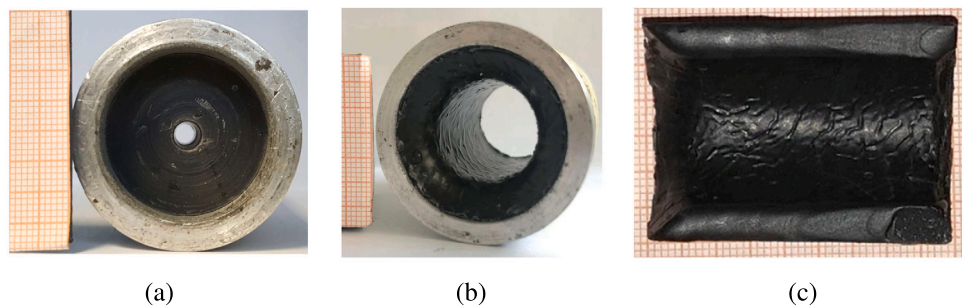
Fig. 5. Paraffin-based fuel (W1): (a,b) head-end views (before and after the firing, respectively) and (c) cross sectional view (after the firing). The oxidizer is direct inward in (a) and (b), rightward in (c). Note the effects of the head-end burning on the strand inlet section.
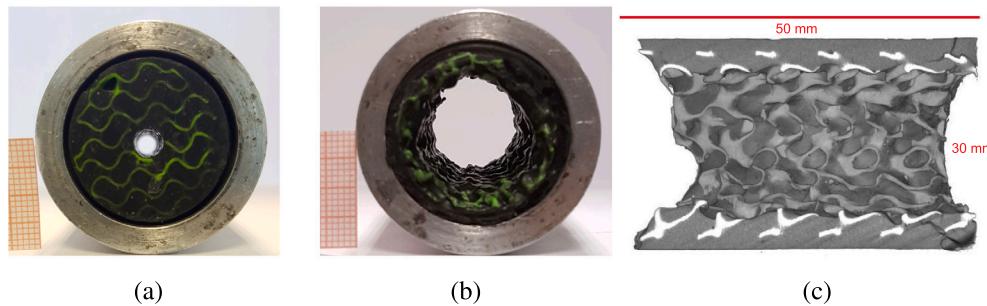

Fig. 6. Armored grain (W1_PLA_i15): (a,b) head-end views (before and after the firing, respectively) and (c) cross sectional view (after the firing). The oxidizer is direct inward in (a) and (b), rightward in (c). In the X-ray tomography (c), the paraffin matrix is in dark gray, the gyroid in light gray.

Table 5
Ballistic tests results of all the investigated fuels: ABS polymeric fuel, paraffin-based formulations and armored grains. Regression rate (r_f) and average oxidizer mass flux ($\bar{G}_{ox}$) are evaluated via DD and MB techniques. Initial fuel port diameter of 5 mm. Nozzle throat diameter of 4 mm, except for the specimens marked with*, in which a 5 mm nozzle was used.

Fuel	Pressure,	Oxidizer, fuel mass flow rate,		Average oxidizer mass flux,		Regression rate,	
	$\bar{p}_c$ [MPa]	$\dot{m}_{ox}$ [g/s]	$\dot{m}_f$ [g/s]	$\bar{G}_{ox,DD}$ [kg/(m² s)]	$\bar{G}_{ox,MB}$ [kg/(m² s)]	$r_{f,DD}$ [mm/s]	$r_{f,MB}$ [mm/s]
ABS	0.86 ± 0.06	5.0	0.96 ± 0.09	47.7 ± 8.6	41.2 ± 4.3	0.37 ± 0.04	0.47 ± 0.04
W1	0.85 ± 0.09	5.0	2.32 ± 0.11	42.5 ± 1.7	36.3 ± 1.4	1.05 ± 0.04	1.21 ± 0.04
S05W1	0.84 ± 0.07	5.0	1.80 ± 0.12	44.2 ± 3.6	37.3 ± 4.0	0.82 ± 0.02	0.95 ± 0.03
S10W1	0.88 ± 0.09	5.0	1.40 ± 0.06	47.1 ± 2.0	39.9 ± 2.4	0.70 ± 0.02	0.81 ± 0.03
W1_PLA_i15	0.88 ± 0.02	5.0	3.76 ± 0.09	41.6 ± 0.5	37.1 ± 0.9	1.62 ± 0.05	1.79 ± 0.04
W1_NY_i15	0.92 ± 0.10	5.0	3.61 ± 0.10	40.5 ± 1.8	35.8 ± 1.4	1.66 ± 0.09	1.84 ± 0.09
W1_ABS_i15	0.86 ± 0.05	5.0	3.69 ± 0.10	37.7 ± 1.1	36.0 ± 0.7	1.80 ± 0.02	1.87 ± 0.04
W1_ABS_i10*	0.57 ± 0.01	5.0	4.77 ± 0.14	30.5 ± 0.9	29.1 ± 1.1	2.15 ± 0.19	2.23 ± 0.13
	0.74 ± 0.04	7.5	7.38 ± 0.45	49.5 ± 1.9	45.3 ± 2.7	3.24 ± 0.13	3.47 ± 0.13
S05W1_ABS_i10*	0.55 ± 0.05	5.0	3.82 ± 0.55	33.2 ± 3.3	31.9 ± 3.2	1.75 ± 0.17	1.81 ± 0.21
	0.75 ± 0.01	7.5	6.06 ± 0.42	57.1 ± 4.8	47.1 ± 1.3	2.62 ± 0.17	3.04 ± 0.09
S10W1_ABS_i10*	0.53 ± 0.06	5.0	2.76 ± 0.25	40.5 ± 5.0	35.6 ± 1.8	1.28 ± 0.14	1.42 ± 0.10
	0.82 ± 0.01	7.5	4.00 ± 0.14	58.5 ± 2.8	46.8 ± 2.1	1.63 ± 0.04	1.94 ± 0.03

5.1. Paraffin-based fuels and armored grains

The regression rate values of paraffin-based formulations and armored grains are shown in Figs. 7(a) and 7(b), respectively. The former chart highlights the fast burning behavior of paraffin-based formulations with respect to the ABS fuel, confirming that the r_f of paraffin fuels is 3–4 times the one of conventional polymeric fuels with vaporization as the only regression mechanism [16,17,37,45]. The latter chart also evidences that the r_f of paraffin fuels can be enhanced by the presence of an inner gyroid reinforcement. For all the formulations in Fig. 7, a systematic difference between the two r_f data reduction techniques is experienced, with the $r_{f,MB}$ exhibiting higher values than $r_{f,DD}$. This gap relies on the fact the DD method is based on the port diameter variation alone and it does not capture head-end burning observed in the fired grains (see Figs. 5 and 6), while the phenomenon is taken into account by the MB method. This difference is more marked in paraffin-based fuels than in armored grains, as testified

by r_f data in Table 5 and the percent r_f variation in Fig. 7(b). In fact, the faster r_f of armored grains with respect to the "not armored counterparts" are lower if considering the MB values rather than the DD ones. This suggests that, under the investigated conditions, armored grains are less prone to head-end burning. Nevertheless, the comparison between $r_{f,MB}$ and $r_{f,DD}$ confirms how both the techniques are suitable for performing relative grading of the fuel ballistic characteristics.

Concerning paraffin fuels in Fig. 7(a) and Table 5, the pure paraffin fuel (W1) exhibits a $r_{f,MB}$ that is 2.6 times the one of the ABS. The addition of 5% and 10% mass fractions of SEBS-MA hinders the regression rate performance enhancement and decreases the $r_{f,MB}$ of 22% and 33% respectively. Similar effects are observed by the $r_{f,DD}$ values. A direct correlation between r_f and melt fuel layer viscosity (η) as evaluated under reference conditions of Table 3 (shear rate 1000 s^{-1}, $T = 150$ °C [15]) is proposed in Fig. 8. The chart reports the power law fittings of $r_{f,DD}$ and $r_{f,MB}$ determined considering data of paraffin fuels
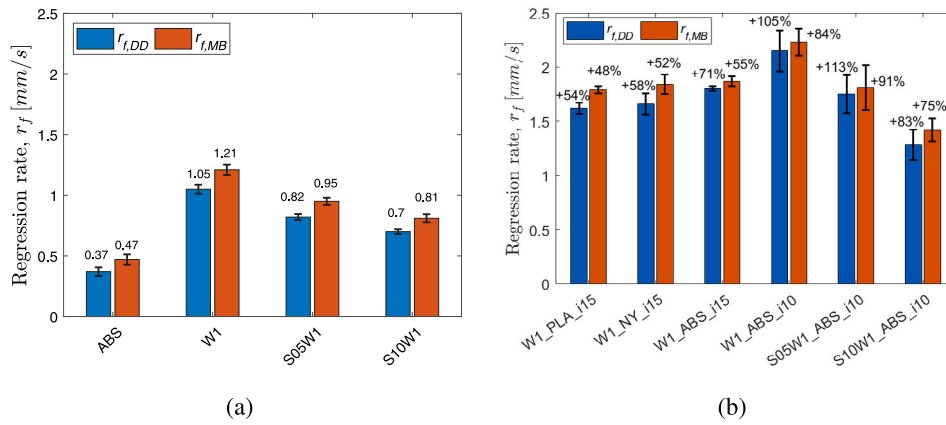
(a)

(b)

Fig. 7. Ballistic performance of (a) ABS and paraffin-based formulations, and (b) armored grains. Error bars are defined by standard deviations, (a) shows absolute r_f values, while (b) reports percent r_f variations of armored grains with respect to the "not armored" counterparts. See Table 5 for experimental conditions.
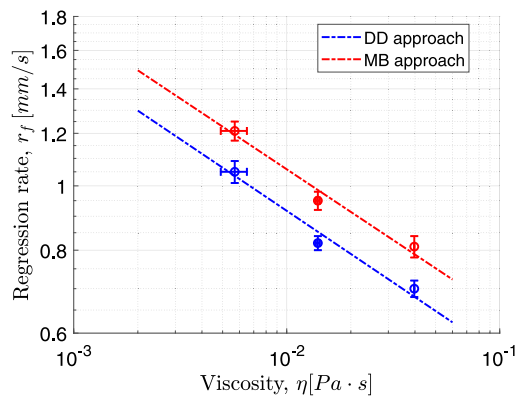

Fig. 8. $r_f(\eta)$ for the paraffin-based fuel formulations: experimental data and power law fitting. Melted fuel viscosity is evaluated at 150 °C and shear rate of 10^3 s^{-1} (Table 3).

from Table 5. Detailed expressions for $r_{f,DD}$ and $r_{f,MB}$ are

$$r_{f,DD} = 0.339 \cdot \eta^{-0.216}, \quad R^2 = 0.974 \quad \text{(DD approach)} \quad (7)$$

$$r_{f,MB} = 0.397 \cdot \eta^{-0.213}, \quad R^2 = 0.976 \quad \text{(MB approach)} \quad (8)$$

It is noteworthy that the two equations feature close exponential coefficient values, while the pre-exponential coefficients differ, with the MB ones being 17% higher than the DD one. This value is related to the percent difference between the $r_{f,MB}$ and the $r_{f,DD}$ of paraffin fuels in Fig. 7(a). The equations are in good agreement with expressions proposed in open literature [60,62,64], in which the exponential coefficient spans from 0.17 to 0.23. Eqs. (7) and (8) underline the importance of rheological analysis to support ballistic behavior preliminary ballistic behavior characterization by melt fuel viscosity under reference conditions.

Considering armored grains in Fig. 7(b) and Table 5, the r_f values are higher than the paraffin waxes ones, despite the reinforcing gyroids are made of slow burning materials (PLA, ABS, NY), as testified by the r_f of ABS. Yet, adding polymers in a gyroid-like shape to the fuel grain does not worsen the ballistic behavior of the paraffin fuel. On the contrary, the embedded gyroid structure enhances the r_f of paraffin fuels in the +48%–+91% range (MB approach), depending on the infill density and the formulation for the paraffin matrix. This suggests that the entrainment mass transfer is not suppressed, though a significant percentage of polymer is present inside the armored grains. The r_f enhancement of armored grains might be caused by the turbulent flow promoted by the burning of the embedded gyroid structure. The

fired armored grain in Fig. 6 exhibits a very rough surface, unlike the traditional straight and smooth surface of a paraffin fuel in Fig. 5. The burned surface of armored grains is still quasi-circular and no slivers of unburned polymer protrude inside the port area. Hence, the gyroid structure burns together with the surrounding paraffin and it produces a rough burning surface that increases the burning surface and promotes the turbulence level. The inner structure could raise the surface skin friction coefficient and the heat feedback to the fuel surface, leading to a boost of the r_f.

The choice of the 3D printer polymer for the gyroid does not significantly affect the regression rate of the armored grains. This is well testified by the r_f values of W1_XX_i15 samples being similar to each other (refer to Fig. 7(b) and Table 5). However, ABS offers the highest $r_{f,DD}$ and $r_{f,MB}$ among the 3D printer polymers. The ballistic performance of W1-based armored grains can be enhanced by using 10% ABS gyroid instead of 15% because of the resulting higher amount of paraffin inside the armored grain. The $r_{f,MB}$ of W1_ABS_i10 is 2.23 mm/s, which is 23% greater than the W1_ABS_i15 one. Hence, the armored grain with ABS gyroid at 10% infill exhibits the highest regression rate.

This ABS_i10 reinforcement was used for armored grains featuring different fuel formulations for the paraffin matrix (refer to XX_ABS_i10 specimens in Fig. 7(b) and Table 5). The same r_f trend of paraffin-based fuels in Fig. 7(a) is also experienced by the armored grains, suggesting that the choice of the paraffin wax and its viscosity impact on the regression rate of armored grains. In fact, the S10W1-based armored grain offers the lowest regression rate ($r_{f,MB}$ = 1.42 mm/s, $r_{f,DD}$ = 1.28 mm/s). The same relative decrements due to SEBS-MA addition are experienced by paraffin-based fuels and by armored grains. In fact, the S10W1 features a $r_{f,MB}$ that is −33% the one of W1; similarly, its armored version (the S10W1_ABS_i10) exhibits a $\Delta r_{f,MB} = -36\%$ with respect to the W1_ABS_i10.

Test conditions for armored grains featuring the ABS_i10 gyroid were varied to inspect the effect of a higher $\bar{G}_{ox}$ on the r_f, as reported in Table 5. The increment of the $\dot{m}_{ox}$ from 5 g/s to 7.5 g/s led to a more vigorous firings. The armored grains experienced $r_{f,MB}$ variations in the +37%–+68% range, with the S10W1_ABS_i10 and the S05W1_ABS_i10 exhibiting the lowest and the highest increments, respectively.

5.2. Regression rate dependence on oxidizer mass flux

The regression rate of solid fuels is strictly dependent of the oxidizer mass flux [5]. Two strategies were followed to evaluate the $r_f(G_{ox})$: performing firings tests at different $\bar{G}_{ox}$ to obtain the corresponding r_f (Section 4.1); tracking the port diameter during the firing via optical method to determine both the r_f and the G_{ox} from high-speed visualizations (Section 4.2).

Table 6

$r_{f,MB}(G_{ox,MB})$ fitting [Eq. (1)] for ABS and paraffin-based formulations.

| Fuel | $r_{f,MB} = a_r \cdot G_{ox,MB}{}^{n_r}$ | | Oxidizer mass flux range, | |
	$a_r \left[\frac{\text{(mm/s)}}{\text{(kg/(m}^2 \text{ s))}^{n_r}}\right]$	n_r	$G_{ox,MB}$ [kg/(m^2 s)]	R^2
ABS	0.133 ± 0.099	0.33 ± 0.19	25–90	0.840
W1	0.092 ± 0.022	0.72 ± 0.06	15–55	0.996
S05W1	0.064 ± 0.021	0.76 ± 0.09	15–55	0.979
S10W1	0.053 ± 0.025	0.75 ± 0.12	20–55	0.969
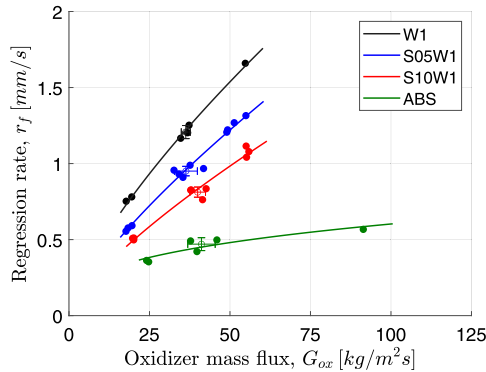
Fig. 9. $r_{f,MB}(G_{ox})$ for ABS and paraffin-based formulations: Circles with error bars are the average $r_{f,MB}$ for firings performed at the same $\bar{G}_{ox,MB} \approx 40$ [kg/(m^2 s)], as reported in Table 5.

5.2.1. Mass-Based approach

Firings at by different $\bar{G}_{ox}$ were performed to estimate the $r_f(G_{ox})$ correlation for the paraffin-based fuels and the ABS. The MB method was used as r_f data reduction technique. The results are illustrated in Fig. 9, where the average $r_{f,MB}$ of Table 5 are also plotted. For each fuel, the fitting coefficients and the R^2 of the $r_{f,MB}(G_{ox})$ power law interpolations are reported in Table 6. The burning time was reduced for an initial port diameter of 5 mm to obtain higher $\bar{G}_{ox}$ (≈ 55 and ≈ 90 kg/(m^2 s) for paraffin-based fuels and ABS, respectively). This enables the investigation of wider $\bar{G}_{ox}$ values than the ones reported in Table 5. Conversely, the initial port was raised to ≈ 15 mm to obtain lower $\bar{G}_{ox}$ (≈ 15 and ≈ 25 kg/(m^2 s) for paraffin-based fuels and ABS, respectively). The fast burning behavior of armored grains prevented from investigating different $\bar{G}_{ox}$. Inspecting higher $\bar{G}_{ox}$ via reducing the Δt_b was not feasible, nor representative of steady combustion, since the burning time of standard tests for armored grains were 4–5 s. As shown in Table 5, the $\dot{m}_{ox}$ was increased to 7.5 g/s and slightly higher $\bar{G}_{ox}$ values were achieved with respect to the tests conducted at 5 g/s. However, the $\bar{G}_{ox}$ were too close to obtain a $r_{f,MB}(G_{ox})$ relation.

Focusing on fuel formulations in Fig. 9 and Table 6, the paraffin-based fuels feature steeper $r_{f,MB}(G_{ox})$ than ABS. Under the investigated conditions, this is a likely consequence of the high radiation heat transfer from ABS combustion. Unlike the majority of the traditional hybrid fuels, ABS exhibits $n_r < 0.50$, with values approaching 0.20 in small HREs (external diameter of 24 mm) [93], such as the SPLab lab-scale HRE. According to Ref. [5], the n_r coefficient is lower under the influence of radiation. The $r_{f,MB}$ values of ABS are notably lower than the paraffin-based ones. The addition of SEBS-MA in the W1 lessens the ballistic response by reducing the a_r, while the n_r is not affected by the presence of SEBS-MA. The fitting coefficients for the fuel formulations are in good agreement with the open literature. The pre-exponential and exponential factors for the W1 are 0.092 and 0.72, and typical a_r and n_r couples for paraffin fuels are: 0.117 and 0.62 [17], 0.081 and 0.73 [45], 0.071 and 0.79 [46]. Concerning ABS, the a_r and n_r in Table 6 are 0.133 and 0.33, and they are comparable with the coefficients found by Bresler ($a_r = 0.103$ and $n_r = 0.22$) [43] and by Oztan ($a_r = 0.127$ and $n_r = 0.37$) [42].

5.2.2. Optical approach

The DD and MB methods provided single average r_f values for each firing. On the contrary, the optical approach returns multiple r_f values for a single firing thanks to the tracking of the port diameter in time. The discrete r_f and the corresponding G_{ox} values from single tests were collected and fitted in one single average $r_f(G_{ox})$ curve for each formulation. At least three videos for each fuel formulation were recorded and analyzed.

The results are reported in Fig. 10, which illustrates the regression rate results of the paraffin-based formulations (Fig. 10(a)) and of the armored grain (Fig. 10(b)) as function of the oxidizer mass flux (G_{ox}). For each formulation, the fitting coefficients and the R^2 of the $r_f(G_{ox})$ power law interpolation are listed in Table 7. Both the DD and the optical method are based on the same concept of sampling the port diameter to retrieve the r_f. The similarity of the two approaches is testified by the good match between the $r_{f,DD}$ results in Table 5 and the corresponding r_f in Fig. 10 at the same $\bar{G}_{ox}$. The circles with error bars in Fig. 10 represent the $r_{f,DD}$ and they are close to the $r_{f,opt}(G_{ox})$ fitting curves.

The n_r coefficients of paraffin formulations and ABS in Table 7 are close to the ones in Table 6, while the a_r values are higher for the MB approach (Table 6) than for the optical approach (Table 7). This is related to the fact that the former approach takes into consideration the head-end burning of the grains, while the latter cannot capture this phenomenon. Nevertheless, the two methodologies present comparable n_r values, confirming the impact of convection and radiation heat transfer on the fuel regression.

Fig. 10 highlights the faster ballistic behavior of armored grains (Fig. 10(b)) with respect the (non-armored) paraffin-based fuels (Fig. 10(a)), the former providing higher r_f than the latter at the same G_{ox}. The armored grains present higher n_r coefficients (0.94–0.98) than paraffin formulations (0.71–0.78). This evidences peculiar features of armored grain during the combustion, leading to a different impact of the G_{ox} on the r_f. The uneven surface of the armored grain (Fig. 6) might be the reason for the high n_r values, as explained in Section 5.2.3. The pre-exponential coefficients for armored grains are higher than those of paraffin fuels, however, the results of S10W1_ABS_i10 and the uncertainties on a_r limit the identification of a general trend.

The G_{ox} ranges in Table 7 for the $r_{f,opt}(G_{ox})$ fitting are different and they depend on the fuel formulations. The slow burning S10W1-based and ABS formulations feature broader G_{ox} intervals compared to the W1 and S05W1 fuels and their corresponding armored grains. This is related to the different ballistic performance of the fuels: faster formulations exhibit significant diameter percent increases and lower G_{ox} values (refer to Eq. (6)), especially at the beginning of the combustion process when the port diameter is small (≈ 5–6 mm). It is worth recalling that the maximum G_{ox} is reached when the port diameter exhibits the lowest value. Moreover, the diameter sampling starts when the flame is stabilized and the burning area is clearly visible, hence the $D(t)$, $r_f(t)$ and $G_{ox}(t)$ at the early stages of the firing are missed.

The different ballistic performance of the fuels can be qualitatively appreciated by looking at the port area evolution of the grains in Figs. 11–13. In the images the red circles are manually tracked by the operator to fit the burning (quasi-) circular port area. Port area variation occurring between two following frames, enables $r_{f,opt}$ and $G_{ox,opt}$ determination based on Eqs. (5) and (6). The combustion image

Table 7

$r_{f,opt}(G_{ox,opt})$ fitting [Eq. (1)] for ABS, paraffin-based formulations and armored grains.

Fuel	$r_{f,opt} = a_r \cdot G_{ox,opt}{}^{n_r}$		Oxidizer mass flux range,	
	$a_r \left[\frac{(mm/s)}{(kg/(m^2 \ s))^{n_r}} \right]$	n_r	$G_{ox,opt}$ [kg/(m^2 s)]	R^2
ABS	0.092 ± 0.017	0.34 ± 0.04	40–190	0.983
W1	0.059 ± 0.022	0.78 ± 0.09	20–70	0.969
S05W1	0.048 ± 0.022	0.75 ± 0.12	20–85	0.976
S10W1	0.038 ± 0.016	0.71 ± 0.09	40–140	0.975
W1_ABS_i10	0.071 ± 0.048	0.98 ± 0.18	15–60	0.979
S05W1_ABS_i10	0.060 ± 0.028	0.93 ± 0.12	15–70	0.984
S10W1_ABS_i10	0.034 ± 0.023	0.94 ± 0.16	25–100	0.982

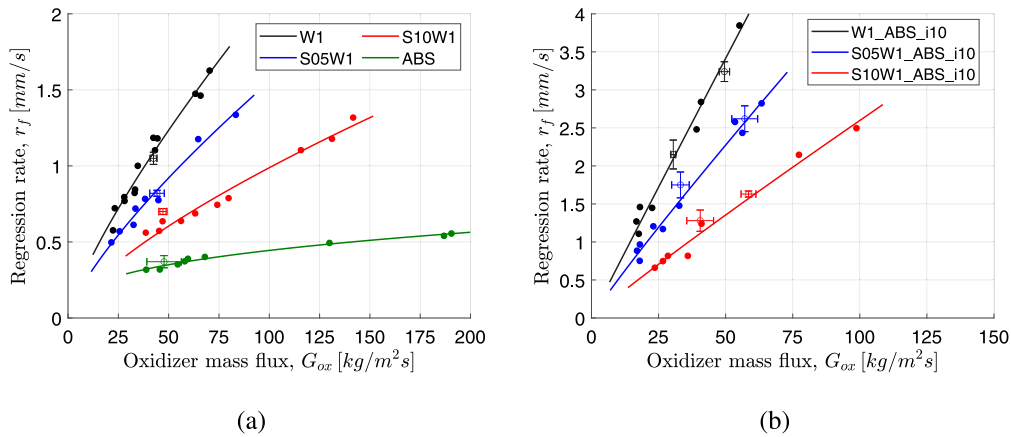(a)   (b)

Fig. 10. $r_{f,opt}(G_{ox,opt})$ by optical technique for (a) ABS and paraffin-based formulations, and (b) armored grains. Points represent the r_f values retrieved from the extracted frames of different firing recordings. Circles with error bars are the average $r_{f,DD}$ of Table 5.
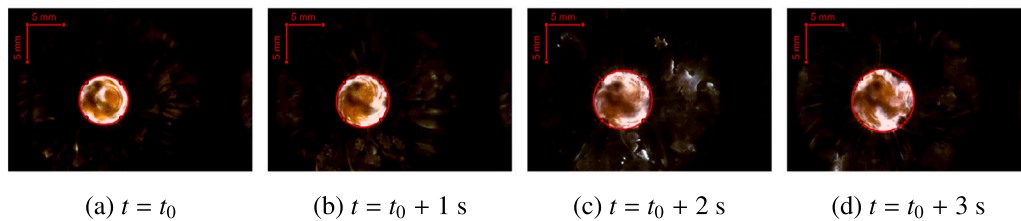

(a) $t = t_0$ (b) $t = t_0 + 1$ s   (c) $t = t_0 + 2$ s   (d) $t = t_0 + 3$ s

Fig. 11. ABS grain combustion evolution. The red circle marks the regressing surface; t_0 is the instant at which the central port is clearly visible and the first diameter is sampled.
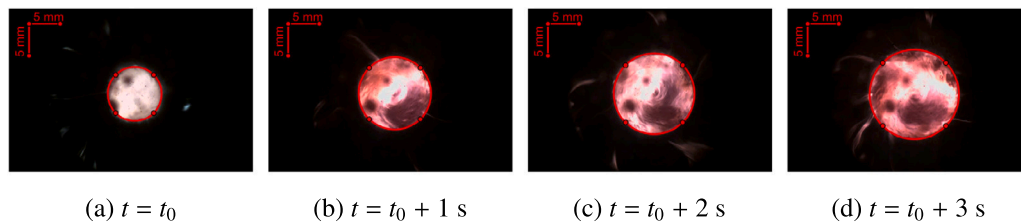

(a) $t = t_0$ (b) $t = t_0 + 1$ s   (c) $t = t_0 + 2$ s   (d) $t = t_0 + 3$ s

Fig. 12. S05W1 grain combustion evolution. The red circle marks the regressing surface; t_0 is the instant at which the central port is clearly visible and the first diameter is sampled.

sequences and the evolution of the burning areas verify the results of Fig. 10 and Table 5: (*i*) ABS is the slowest burning fuel (Fig. 11), (*ii*) the paraffin based fuels burn faster than the polymeric fuels (Fig. 12 vs. Fig. 11), (*iii*) the regression rate of paraffin formulations is boosted in the "armored configuration" (Fig. 12 vs. Fig. 13). The image sequences show the presence of flame flares, confirming the sample head-end burning. The flame flickering and the head-end burning sometimes make the identification and sampling of the port diameter challenging. This is especially true for armored grains, whose burning surfaces are irregular (Fig. 13). On the contrary, the port diameters of ABS and S05W1 can be easily identified and tracked (Figs. 11 and 12).

5.2.3. Considerations about ballistic coefficients of armored grains

The classical Marxman's diffusion-limited theory is commonly used to describe the combustion behavior of solid fuels for HRE [5,26–29]. This theory was developed for fuels that are assumed to pyrolyze and vaporize, and it is not accurate for liquefying fuels, such as paraffin wax. However, it is still the reference theory to design hybrid systems. For the sake of simplicity, we take the Marxman's classical theory as the baseline in our considerations about the ballistic coefficients of armored grains.

According to Marxman, the convective heat flux causes the solid fuel regression. Under the assumptions of (i) turbulent boundary-layer
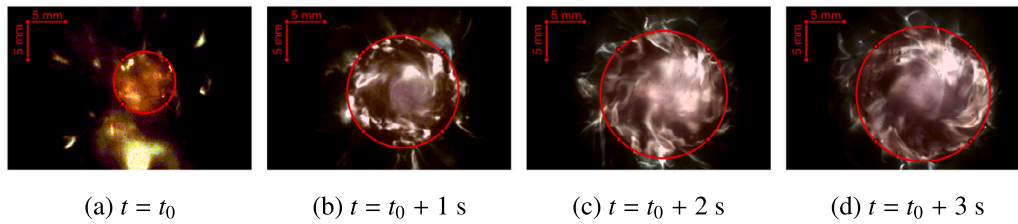
(a) $t = t_0$ (b) $t = t_0 + 1$ s   (c) $t = t_0 + 2$ s   (d) $t = t_0 + 3$ s

Fig. 13. S05W1_ABS_i10 grain combustion evolution. The red circle marks the regressing surface; t_0 is the instant at which the central port is clearly visible and the first diameter is sampled.

flow over the entire fuel, (ii) unit Lewis and Prandtl numbers, and (iii) Reynolds analogy, it is possible to write the energy balance at the regressing surface of the solid fuel [26]:

$$\rho_f \cdot r_f = \frac{c_f}{2} \rho_e u_e \frac{u_e}{u_b} \frac{\Delta h}{h_v} \tag{9}$$

The c_f is the skin friction coefficient in presence of blowing from the regressing surface, the Δh is the enthalpy difference between the flame zone and the fuel surface, the h_v effective heat of gasification, the b and e subscripts indicate that the quantity is evaluated at the flame and at free stream conditions, respectively. The blowing parameter B is introduced and it accounts for the blowing generated by the vaporizing fuel inside the boundary layer.

$$B = \frac{u_e}{u_b} \frac{\Delta h}{h_v} \tag{10}$$

Eq. (10) and the local mass flux due to both the oxidizer and the fuel ($G_{ox} + G_f = \rho_e u_e$) are used to modify Eq. (9) in:

$$\rho_f \cdot r_f = \frac{c_f}{2} (G_{ox} + G_f) \cdot B \tag{11}$$

The friction coefficient can be calculated using empirical relation and Marxman used the expression for turbulent flow over a smooth flat-plate in absence of blowing (Schlichting relations [94]):

$$\frac{c_{f_0}}{2} = 0.03 \, Re_x^{-0.2} \tag{12}$$

where the subscript 0 distinguishes the reference flat-plate value from the blowing surface case c_f. In Eq. (12) the local Reynolds number Re_x is introduced and it is evaluated by knowing the free stream properties and the axial distance x from the grain leading edge.

$$Re_x = \frac{\rho_e u_e x}{\eta_e} \tag{13}$$

Substituting Eqs. (12) and (13) into Eq. (11) produces

$$\begin{aligned} \rho_f \cdot r_f &= 0.03 \frac{c_f}{c_{f_0}} \left(\frac{\rho_e u_e x}{\eta_e} \right)^{-0.2} (G_{ox} + G_f) \cdot B \\ &= 0.03 \frac{c_f}{c_{f_0}} \left(\frac{x}{\eta_e} \right)^{-0.2} (G_{ox} + G_f)^{0.8} \cdot B \end{aligned} \tag{14}$$

The c_f / c_{f_0} ratio is expressed as a function of B [5,26–29], hence the Eq. (14) is shortened to:

$$r_f = A (G_{ox} + G_f)^{0.8} x^{-0.2} \tag{15}$$

The evaluation of Eq. (15) requires the knowledge of $G_{ox} + G_f(r_f)$, that in turn depends on r_f. Therefore, for practical use the simplified Eq. (1) is usually preferred.

Among the hypotheses made by Marxman there is the turbulent flow over a flat-plate (refer to Eq. (12)). The theory of hybrid does not take into account the roughness of the fuel surface, that is an important feature of the armored grain. Still, the roughness of the armored grains may invalidate the assumption of flat surface and Eq. (12). For very rough pipes, if the Reynolds number based on the diameter is high enough for the flow to be considered turbulent, then the friction factor becomes independent of both the length-based and diameter-based Reynolds number [95]. In this case, if the flow is fully developed, the

c_f depends only on the ratio between the characteristic height of the roughness and the diameter. In analogy to the Marxman's model based on turbulent boundary-layer flow over a flat plate, the friction factor for rough plates is independent of Re_x and its value is given by ratio between the thickness of the boundary layer and the characteristic height of the roughness [94]. The extreme rough burning surface of armored grains suggest the use of a friction factor for rough plates or pipes. In both cases, it can be considered independent of the Reynolds number, and Eq. (12) should be replaced with $c_{f_0} \propto Re_x^0$, in turn leading to:

$$r_f = A (G_{ox} + G_f) \tag{16}$$

Despite strong assumptions are present in both the Marxman's theory and its modified version for armored grains, the comparison between Eqs. (15) and (16) highlights that armored grains characterized by a rough the burning surface (see Fig. 6) are more sensitive to $(G_{ox} + G_f)$, hence to G_{ox}, than traditional fuels with smooth burning surface, such as paraffin-based fuels (see Fig. 5). This is confirmed by the exponential coefficients in Table 7. In fact, the n_r coefficients for armored grains are in the 0.93–0.98 range, while the paraffin-based in the 0.71–0.78. These values are close to 1 and 0.8, that are the exponential factors of the mass flux in Eqs. (16) and (15).

5.3. Further considerations on slump of fuels

One critical aspect of paraffin fuels is represented by the slump under storage and operating conditions (e.g. launch phases, throttling, shutdown and re-ignitions), especially at elevated temperatures [96]. This phenomenon could occasionally occur during combustion tests of paraffin-based fuels as reported in Fig. 14. This is mainly due to the softening of paraffin at high temperatures and the presence of manu-facturing flaws, such as voids, caused by the paraffin shrinkage [97]. Despite the possible presence of imperfections even in the armored grains, the paraffin slump was not observed during the armored grain combustion. In fact, the inner reinforcement prevents the detachment of paraffin chunks during combustion and the central port of armored grains remains always quasi circular (refer to the sequence of images in Fig. 13). This confirms the findings of Armold [75], who successfully limited the paraffin slumping by adding acrylic honeycomb structures to the fuel grain.

6. Conclusions and future developments

The armored grain, a paraffin grain embedding a 3D printed gyroid structure for structural enhancement, was investigated and proposed as an alternative to paraffin-based fuels. Pre-burning characterization of armored grains was presented in a companion paper [22]. The present work focuses on the ballistic behavior of armored grains, which has not been deeply investigated in the open literature yet. The ballistic characterization involved paraffin formulations and armored grains and it was conducted in the lab-scale HRE with gaseous oxygen as oxidizer. Paraffin formulations were based on a micro-crystalline wax in the pure and blended form with 5 wt% and 10 wt% of SEBS-MA. In the armored grains, the different paraffin formulations were combined with a 3D
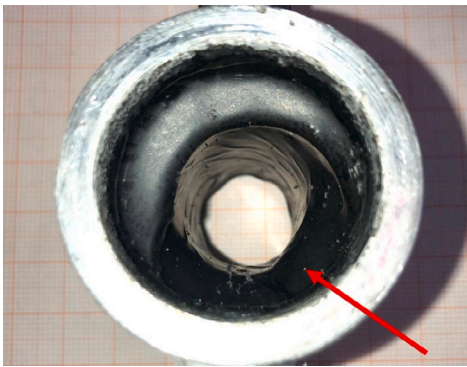
Fig. 14. The slump of a paraffin-based fuel grain. The oxidizer flow is direct inward.

printed gyroid in polylactic acid (PLA), acrylonitrile butadiene styrene (ABS), and nylon 6 (NY) at 10% and 15% infill.

The evaluation of the ballistic performance was assessed by measuring the regression rate (r_f) of the fuels via mass-based (MB) and geometry-based (DD) thickness over time approaches. The firing times were chosen according to the fuel formulation to reach the same average oxidizer mass flux ($\bar{G}_{ox}$), which is the key parameter for the r_f. The faster burning behavior of paraffin fuels compared to polymeric fuels was confirmed by the firing tests. The $r_{f,MB}$ of pure wax was 2.6-fold higher than the $r_{f,MB}$ of ABS. The addition of SEBS-MA to the pure wax reduced the ballistic performance: 5% and 10% mass fractions of the polymer led to −22% and −33% $r_{f,MB}$ reductions. The drop of the r_f was explained by the increment of the melted fuel viscosity and the $r_f(\eta)$ relation was retrieved.

The firing tests on armored grains revealed that these fuels burn faster than the (unblended and blended) paraffin formulations, even though the polymers employed for the 3D printed reinforcements (PLA, ABS, NY) are slow-burning materials. This was explained by the uneven and irregular texture of the burning surface that promotes turbulence and convective heat transfer. Moreover, the presence of a reinforcement did not alter the viscosity of the paraffin matrix, hence the entrainment is not hindered. Changing the polymer for the reinforcement slightly altered the r_f and the ABS provided the best results. Considering the ABS gyroid with 15% infill, the $r_{f,MB}$ of W1 was enhanced by 55%, while the use of PLA and NY resulted in 48% and 52% increments, respectively. The reduction of the infill fraction of the ABS gyroid from 15% to 10% improved the r_f. The presence of SEBS-MA in the paraffin matrix of the armored grains reduced the r_f, and the same relative decrements due to SEBS-MA observed for the paraffin formulations were also experienced by the armored grains.

The regression rate dependence on the oxidizer mass flux was investigated via tests at different $\bar{G}_{ox}$ and via an optical approach. Firing tests were also recorded by a high-speed camera, that tracked the port area evolution during the combustion. The $r_f(G_{ox})$ trends observed for the fuels confirmed the fast burning behavior of armored grains with respect to paraffin fuels, the negative impact of SEBS-MA on both the two fuel families, and the low ballistic performance of ABS. The coefficients of the $r_f(G_{ox})$ correlations for paraffin fuels and ABS were found to be in agreement with open literature. The higher amount of SEBS-MA in the paraffin fuels reduced the pre-exponential factor, while the exponential coefficients were not significantly changed and they were in the 0.72–0.76 and 0.71–0.79 ranges for the MB and the optical approaches, respectively. The same impact of SEBS-MA on the $r_f(G_{ox})$ was also observed for armored grains, that presented greater dependence on the G_{ox} than the paraffin-based fuels. In fact, the exponential coefficients were around 0.93–0.98. This behavior was explained by revising the friction coefficient used in the Marxman's theory to consider the characterizing rough burning surface of armored grains.

The findings of the present work show that the armored grain concept is a paraffin fuels reinforcement strategy that not only saves the entrainment, but also provides an augmented regression rate for paraffin-based fuels. The ballistic results and the promising structural behavior that was previously assessed in [22] make the armored grain an effective solution for the long-standing research for green paraffin-based fuels featuring both structural and combustion performance. The main features of hybrid rocket propulsion based on paraffin fuels could be fully exploited and the inherent drawbacks of this technology overcome thanks to the armored grain approach.

Further studies are needed to explore the features of this new concept, especially from the ballistic perspective. Numerical simulations of the motion field induced by the reinforcement embedded in the solid grain should be carried out to inspect the fluid dynamic inside the combustion chamber. The computational fluid dynamics (CFD) analysis would start from the X-ray tomography of the burned fuel grains. Further firing tests under different operating conditions (quasi-steady and throttling) would provide a wider data-set for a better comprehension of the combustion mechanism of armored grains. The next studies will focus on the scale-up of armored grains to assess their ballistic performance under operating conditions closer to actual flying systems.

Declaration of competing interest

The authors declare that they have no known competing financial interests or personal relationships that could have appeared to influence the work reported in this paper.

Funding

References

[1] D. Altman, Overview and history of hybrid rocket propulsion, in: M.J. Chiaverini, K.K. Kuo (Eds.), Fundamentals of Hybrid Rocket Combustion and Propulsion, AIAA, 2007, pp. 1–36, http://dx.doi.org/10.2514/5.9781600866876.0001.0036, Ch. 1.

[2] A. Ruffin, E. Paccagnella, M. Santi, F. Barato, D. Pavarin, Real-time deep throttling tests of a hydrogen peroxide hybrid rocket motor, J. Propul. Power 38 (5) (2022) 833–848, http://dx.doi.org/10.2514/1.B38504.

[3] Z. Zhao, G. Cai, B. Zhao, Y. Liu, N. Yu, Experimental investigation of a flow-oriented throttleable injector designed for throttleable hybrid rocket motor, Acta Astronaut. 192 (2022) 122–132, http://dx.doi.org/10.1016/j.actaastro.2021.12.024.

[4] H. Tian, X. Meng, H. Zhu, C. Li, R. Yu, Y. Zhang, G. Cai, Dynamic characteristics study of regression rate in variable thrust hybrid rocket motor, Acta Astronaut. 193 (2022) 221–229, http://dx.doi.org/10.1016/j.actaastro.2022.01.006.

[5] M.J. Chiaverini, Review of solid-fuel regression rate behavior in classical and nonclassical hybrid rocket motors, in: M.J. Chiaverini, K.K. Kuo (Eds.), Fundamentals of Hybrid Rocket Combustion and Propulsion, AIAA, 2007, pp. 37–126, http://dx.doi.org/10.2514/5.9781600866876.0037.0126, Ch. 2.

[6] D. Pastrone, Approaches to low fuel regression rate in hybrid rocket engines, Int. J. Aerosp. Eng. 2012 (649753) (2012) 1–12, http://dx.doi.org/10.1155/2012/649753.

[7] H. Zhu, M. Li, H. Tian, P. Wang, N. Yu, G. Cai, Numerical and experimental investigations on injection effects of orifice injector plate in hybrid rocket motors, Acta Astronaut. 162 (2019) 275–283, http://dx.doi.org/10.1016/j.actaastro.2019.06.002.

[8] H. Tian, X. Jiang, R. Yu, H. Zhu, Y. Zhang, G. Cai, Numerical analysis of the hybrid rocket motor with axial injection based on oxidizer flow distribution, Acta Astronaut. 192 (2022) 245–257, http://dx.doi.org/10.1016/j.actaastro.2021.12.025.

[9] M. Bouziane, A. Bertoldi, P. Milova, P. Hendrick, M. Lefebvre, Performance comparison of oxidizer injectors in a 1-kN paraffin-fueled hybrid rocket motor, Aerosp. Sci. Technol. 89 (2019) 392–406, http://dx.doi.org/10.1016/j.ast.2019.04.009.

[10] S. Yuasa, K. Yamamoto, H. Hachiya, K. Kitagawa, Y. Oowada, Development of a small sounding hybrid rocket with a swirling-oxidizer-type engine, in: 37th Jt. Propuls. Conf. Exhib., Salt Lake City, UT, 2009, pp. 1–7, http://dx.doi.org/10.2514/6.2001-3537.

[11] B. Vignesh, R. Kumar, Effect of multi-location swirl injection on the performance of hybrid rocket motor, Acta Astronaut. 176 (2020) 111–123, http://dx.doi.org/10.1016/j.actaastro.2020.06.029.

[12] W.H. Knuth, M.J. Chiaverini, J.A. Sauer, D.J. Gramer, Solid-fuel regression rate behavior of vortex hybrid rocket engines, J. Propul. Power 18 (3) (2002) 600–609, http://dx.doi.org/10.2514/2.5974.

[13] D.M. Gibbon, G.S. Haag, Investigation of an Alternative Geometry Hybrid Rocket for Small Spacecraft Orbit Transfer, Tech. Rep. AD No. 393398, Surrey Satellite Technology Ltd., Guildford, United Kingdom, 2001, DTIC Tech..

[14] C. Paravan, J. Glowacki, S. Carlotti, F. Maggi, L. Galfetti, Vortex combustion in a lab-scale hybrid rocket motor, in: 2018 Jt. Propuls. Conf., Salt Lake City, UT, 2016, pp. 1–21, http://dx.doi.org/10.2514/6.2016-4562.

[15] C. Paravan, L. Galfetti, C. Paravan, R. Bisin, F. Piscaglia, Combustion processes in hybrid rockets, Int. J. Energ. Mater. Chem. Propul. 18 (3) (2019) 255–286, http://dx.doi.org/10.1615/intjenergeticmaterialschemprop.2019027834.

[16] M.A. Karabeyoglu, D. Altman, B.J. Cantwell, Combustion of liquefying hybrid propellants: Part 1, General theory, J. Propul. Power 18 (3) (2002) 610–620, http://dx.doi.org/10.2514/2.5975.

[17] M.A. Karabeyoglu, G. Zilliac, B.J. Cantwell, S. DeZilwa, P. Castellucci, Scale-up tests of high regression rate paraffin-based hybrid rocket fuels, J. Propul. Power 20 (6) (2004) 1037–1045, http://dx.doi.org/10.2514/1.3340.

[18] C. Paravan, R. Bisin, S. Carlotti, F. Maggi, L. Galfetti, Diagnostics for entrainment characterization in liquefying fuel formulations, in: 54st AIAA/SAE/ASEE Jt. Propuls. Conf., 2018, pp. 1–12, http://dx.doi.org/10.2514/6.2018-4663.

[19] R. Bisin, C. Paravan, S. Alberti, L. Galfetti, An innovative strategy for paraffin-based fuels reinforcement: Part I, Mechanical and pre-burning characterization, in: 8th Eur. Conf. for Aeronaut. and Space Sci., EUCASS, Madrid, ES, 2019, pp. 1–14, http://dx.doi.org/10.13009/EUCASS2019-718.

[20] R. Bisin, C. Paravan, A. Verga, L. Galfetti, An innovative strategy for paraffin-based fuels reinforcement: Part II, Ballistic characterization, in: 8th Eur. Conf. for Aeronaut. and Space Sci., EUCASS, Madrid, ES, 2019, pp. 1–9, http://dx.doi.org/10.13009/EUCASS2019-728.

[21] R. Bisin, C. Paravan, S. Parolini, L. Galfetti, Impact of 3D-printing on the mechanical reinforcement and the ballistic response of paraffin-based fuels: the armored grain, in: AIAA Propul. Energy 2020 Forum, Virtual Event, 2020, pp. 1–21, http://dx.doi.org/10.2514/6.2020-3735.

[22] R. Bisin, C. Paravan, S. Alberti, L. Galfetti, A new strategy for the reinforcement of paraffin-based fuels based on cellular structures: The armored grain – mechanical characterization, Acta Astronaut. 176 (Nov. 2020) 494–509, http://dx.doi.org/10.1016/j.actaastro.2020.07.003.

[23] R. Bisin, A. Verga, D. Bruschi, C. Paravan, Strategies for paraffin-based fuels reinforcement: 3D printing and blending with polymers, in: AIAA Propul. Energy 2021 Forum, Virtual Event, 2021, pp. 1–20, http://dx.doi.org/10.2514/6.2021-3502.

[24] A.H. Schoen, Infinite Periodic Minimal Surface without Self-Intersections, Electron. Res. Cent., Camb., MA, May, 1970, NASA TN D-5541.

[25] S. Heister, E. Wernimont, Hydrogen peroxide, hydroxyl ammonium nitrate, and other storable oxidizers, in: M.J. Chiaverini, K.K. Kuo (Eds.), Fundamentals of Hybrid Rocket Combustion and Propulsion, AIAA, 2007, pp. 457–488, http://dx.doi.org/10.2514/5.9781600866876.0457.0488, Ch. 11.

[26] T. Marquardt, J. Majdalani, Review of classical diffusion-limited regression rate models in hybrid rockets, Aerosp. 6 (6) (2019) 75, http://dx.doi.org/10.3390/aerospace6060075.

[27] G. Marxman, M. Gilbert, Turbulent boundary layer combustion in the hybrid rocket, Symp. (Int.) Combust. 9 (1) (1963) 371–383, http://dx.doi.org/10.1016/S0082-0784(63)80046-6.

[28] G.A. Marxman, C.E. Wooldridge, R.J. Muzzy, Fundamentals of hybrid boundary-layer combustion, Prog. Astronaut. Rocket. 15 (1964) 485–522, http://dx.doi.org/10.1016/B978-1-4832-2730-6.50025-7.

[29] G.A. Marxman, Combustion in the turbulent boundary layer on a vaporizing surface, Symp. (Int.) Combust. 10 (1) (1965) 1337–1349, http://dx.doi.org/10.1016/S0082-0784(65)80268-5.

[30] V. Tyurenkova, M. Smirnova, Material combustion in oxidant flows: Self-similar solutions, Acta Astronaut. 120 (2016) 129–137, http://dx.doi.org/10.1016/j.actaastro.2015.11.033.

[31] V.V. Tyurenkova, L.I. Stamov, Flame propagation in weightlessness above the burning surface of material, Acta Astronaut. 159 (2019) 342–348, http://dx.doi.org/10.1016/j.actaastro.2019.03.053.

[32] V. Betelin, A. Kushnirenko, N. Smirnov, V. Nikitin, V. Tyurenkova, L. Stamov, Numerical investigations of hybrid rocket engines, Acta Astronaut. 144 (2018) 363–370, http://dx.doi.org/10.1016/j.actaastro.2018.01.009.

[33] A. Kushnirenko, L. Stamov, V. Tyurenkova, M. Smirnova, E. Mikhalchenko, Three-dimensional numerical modeling of a rocket engine with solid fuel, Acta Astronaut. 181 (2021) 544–551, http://dx.doi.org/10.1016/j.actaastro.2021.01.028.

[34] G.A. Risha, Metals, energetic additives, and special binders used in solid fuels for hybrid rockets, in: M.J. Chiaverini, K.K. Kuo (Eds.), Fundamentals of Hybrid Rocket Combustion and Propulsion, AIAA, 2007, pp. 413–456, http://dx.doi.org/10.2514/5.9781600866876.0413.0456, Ch. 10.

[35] T.L. Connell, R.A. Yetter, G.A. Risha, Z.J. Huba, A. Epshteyn, B.T. Fisher, Enhancement of solid fuel combustion in a hybrid rocket motor using amorphous Ti-Al-B nanopowder additives, J. Propul. Power 35 (3) (2019) 662–665, http://dx.doi.org/10.2514/1.B37330.

[36] C. Paravan, Nano-sized and mechanically activated composites: Perspectives for enhanced mass burning rate in aluminized solid fuels for hybrid rocket propulsion, Aerospace 12 (6) (2019) 1–31, http://dx.doi.org/10.3390/aerospace6120127.

[37] M.A. Karabeyoglu, B.J. Cantwell, Combustion of liquefying hybrid propellants: Part 2, stability of liquid films, J. Propul. Power 18 (3) (2002) 621–630, http://dx.doi.org/10.2514/2.5976.

[38] M.A. Karabeyoglu, B.J. Cantwell, G. Zilliac, Development of scalable space-time averaged regression rate expressions for hybrid rockets, J. Propul. Power 23 (4) (2007) 737–747, http://dx.doi.org/10.2514/1.19226.

[39] B. Greiner, R. Frederick Jr., Results of labscale hybrid rocket motor investigation, in: 28th Jt. Propuls. Conf. Exhib, Nashville,TN, 1992, pp. 1–14, http://dx.doi.org/10.2514/6.1992-3301.

[40] J. Rabinovitch, E.T. Jens, A.C. Karp, B. Nakazono, A. Conte, D.A. Vaughan, Characterization of PolyMethylMethAcrylate as a fuel for hybrid rocket motors, in: 2018 Jt. Propuls. Conf., Cincinnati, OH, 2018, pp. 1–21, http://dx.doi.org/10.2514/6.2018-4530.

[41] S.A. Whitmore, Z.W. Peterson, S.D. Eilers, Comparing hydroxyl terminated polybutadiene and acrylonitrile butadiene styrene as hybrid rocket fuels, J. Propul. Power 29 (3) (2013) 582–592, http://dx.doi.org/10.2514/1.B34382.

[42] C. Oztan, E. Ginzburg, M. Akin, Y. Zhou, R.M. Leblanc, V. Coverstone, 3D printed ABS/Paraffin hybrid rocket fuels with carbon dots for superior combustion performance, Combust. Flame 225 (2021) 428–434, http://dx.doi.org/10.1016/j.combustflame.2020.11.024.

[43] J.A. Bresler, B. Natan, Experimental investigation of ABS-paraffin 3D printed hybrid rocket fuels, in: AIAA Propul. Energy 2019 Forum, Indianapolis, IN, 2019, pp. 1–16, http://dx.doi.org/10.2514/6.2019-4094.

[44] M. McFarland, E. Antunes, Small-scale static fire tests of 3D printing hybrid rocket fuel grains produced from different materials, Aerosp. 6 (7) (2019) 81, http://dx.doi.org/10.3390/aerospace6070081.

[45] A. Karabeyoglu, B. Cantwell, J. Stevens, Evaluation of the homologous series of normal alkanes as hybrid rocket fuels, in: 41th AIAA/ASME/SAE/ASEE Jt. Propuls. Conf. Exhib., Tucson, AZ, 2005, pp. 1–42, http://dx.doi.org/10.2514/6.2005-3908.

[46] G.D. Di Martino, S. Mungiguerra, C. Carmicino, R. Savino, D. Cardillo, F. Battista, M. Invigorito, G. Elia, Two-hundred-Newton laboratory-scale hybrid rocket testing for paraffin fuel-performance characterization, J. Propul. Power 35 (1) (2019) 224–235, http://dx.doi.org/10.2514/1.B37017.

[47] P. George, S. Krishnan, P.M. Varkey, M. Ravindran, L. Ramachandran, Fuel regression rate in hydroxyl-terminated-polybutadiene/gaseous-oxygen hybrid rocket motors, J. Propul. Power 17 (1) (2001) 35–42, http://dx.doi.org/10.2514/2.5704.

[48] B. Evans, N. Favorito, K. Kuo, Study of solid fuel burning-rate enhancement behavior in an X-ray translucent hybrid rocket motor, in: 41th AIAA/ASME/SAE/ASEE Jt. Propuls. Conf. Exhib., Tucson, AZ, 2005, pp. 1–12, http://dx.doi.org/10.2514/6.2005-3909.

[49] K. Kosaka, S. Suzuki, D. Fukuma, A. Yamamoto, H. Maruizumi, Development of HTPB binder for solid propellant, in: 24th Jt. Propuls. Conf., Boston, MA, 1988, pp. 1–5, http://dx.doi.org/10.2514/6.1988-3352.

[50] J. DeSain, B. Brady, K. Metzler, T. Curtiss, T. Albright, Tensile tests of paraffin wax for hybrid rocket fuel grains, in: 45th AIAA/ASME/SAE/ASEE Jt. Propuls. Conf. Exhib., Denver, CO, 2009, pp. 1–27, http://dx.doi.org/10.2514/6.2009-5115.

[51] K. Veale, S. Adali, J. Pitot, C. Bemont, The structural properties of paraffin wax based hybrid rocket fuels with aluminium particles, Acta Astronaut. 151 (2018) 864–873, http://dx.doi.org/10.1016/j.actaastro.2018.07.042.

[52] S. Sisi, A. Gany, Combustion of plain and reinforced paraffin with nitrous oxide, Int. J. Energ. Mater. Chem. Propul. 14 (4) (2015) 331–345, http://dx.doi.org/10.1615/IntJEnergeticMaterialsChemProp.2015011139.

[53] S.N. Mahottamananda, N.P. Kadiresh, Mechanical characteristics of paraffin wax-HTPB based hybrid rocket fuel, in: Proc. Int. Conf. of Aerosp. Mech. Eng. 2019, 2020, pp. 91–103, http://dx.doi.org/10.1007/978-981-15-4756-0_9.

[54] S.N. Mahottamananda, N.P. Kadiresh, Y. Pal, Regression rate characterization of HTPB-paraffin based solid fuels for hybrid rocket, Propellants Explos. Pyrotech. 45 (11) (2020) 1755–1763, http://dx.doi.org/10.1002/prep.202000051.

[55] J.C. Thomas, C. Paravan, J.M. Stahl, A.J. Tykol, F.A. Rodriguez, L. Galfetti, E.L. Petersen, Experimental evaluation of HTPB/paraffin fuel blends for hybrid rocket applications, Combust. Flame 229 (2021) 111386, http://dx.doi.org/10.1016/j.combustflame.2021.02.032.

[56] Y. Matsumoto, K. Takahashi, K. Kinoshita, K. Nakajima, Characteristics of a polymeric as an additive in WAX-based hybrid rocket fuel, in: 2018 Jt. Propuls. Conf., Cincinnati, OH, 2018, pp. 1–9, http://dx.doi.org/10.2514/6.2018-4595.

[57] S. Kim, H. Moon, J. Kim, J. Cho, Evaluation of paraffin polyethylene blends as novel solid fuel for hybrid rockets, J. Propul. Power 31 (6) (2015) 1750–1760, http://dx.doi.org/10.2514/1.B35565.

[58] S. Maruyama, T. Ishiguro, K. Shinohara, I. Nakagawa, Study on mechanical characteristic of paraffin-based fuel, in: 47th AIAA/ASME/SAE/ASEE Jt. Propuls. Conf. Exhib., San Diego, CA, 2011, pp. 1–9, http://dx.doi.org/10.2514/6.2011-5678.

[59] R. Kumar, P.A. Ramakrishna, Studies on EVA-based wax fuel for launch vehicle applications, Propellants Explos. Pyrotech. 41 (2) (2016) 295–303, http://dx.doi.org/10.1002/prep.201500172.

[60] C. Paravan, L. Galfetti, F. Maggi, A critical analysis of paraffin-based fuel formulations for hybrid rocket propulsion, in: 53rd AIAA/SAE/ASEE Jt. Propuls. Conf., Atlanta, GA, 2017, pp. 1–17, http://dx.doi.org/10.2514/6.2017-4830.

[61] D. Mengu, R. Kumar, Development of EVA-SEBS based wax fuel for hybrid rocket applications, Acta Astronaut. 152 (2018) 325–334, http://dx.doi.org/10.1016/j.actaastro.2018.08.034.

[62] M. Kobald, C. Schmierer, H.K. Ciezki, S. Schlechtriem, E. Toson, L.T. De Luca, Viscosity and regression rate of liquefying hybrid rocket fuels, J. Propul. Power 33 (5) (2017) 1245–1251, http://dx.doi.org/10.2514/1.B36207.

[63] Y. Tang, S. Chen, W. Zhang, R. Shen, L.T. DeLuca, Y. Ye, Mechanical modifications of paraffin-based fuels and the effects on combustion performance, Propellants Explos. Pyrotech. 42 (11) (2017) 1268–1277, http://dx.doi.org/10.1002/prep.201700136.

[64] T. Ishigaki, I. Nakagawa, Improving physical properties of wax-based fuels and its effect on regression rate, J. Propul. Power 36 (1) (2020) 123–128, http://dx.doi.org/10.1002/prep.201700136.

[65] C. Oztan, V. Coverstone, Utilization of additive manufacturing in hybrid rocket technology: A review, Acta Astronaut. 180 (2021) 130–140, http://dx.doi.org/10.1016/j.actaastro.2020.11.024.

[66] S.A. Whitmore, S.L. Merkley, L. Tonc, S.D. Mathias, Survey of selected additively manufactured propellants for arc ignition of hybrid rockets, J. Propul. Power 32 (6) (2016) 1494–1504, http://dx.doi.org/10.2514/1.B36106.

[67] T. Mayer, B. Bartkowiak, Scalability analysis of additively manufactured grain for 4 kN high test peroxide hybrid rocket motor, in: 8th Eur. Conf. for Aeronaut. and Space Sci., EUCASS, Madrid, ES, 2019, pp. 1–12, http://dx.doi.org/10.13009/EUCASS2019-979.

[68] M.J. Degges, P. Taraschi, J. Syphers, D. Armold, J.E. Boyer, K. Kuo, Student investigation of rapid prototyping technology for hybrid rocket motor fuel grains, in: 49th AIAA/ASME/SAE/ASEE Jt. Propuls. Conf., San Jose, CA, 2013, pp. 1–12, doi:https://arc.aiaa.org/doi/abs/10.2514/6.2013-4016.

[69] S.A. Whitmore, S.D. Walker, D.P. Merkley, M. Sobbi, High regression rate hybrid rocket fuel grains with helical port structures, J. Propul. Power 31 (6) (2015) 1727–1738, http://dx.doi.org/10.2514/1.B35615.

[70] S.A. Whitmore, S.D. Walker, Engineering model for hybrid fuel regression rate amplification using helical ports, J. Propul. Power 33 (2) (2017) 398–407, http://dx.doi.org/10.2514/1.B36208.

[71] A.W. Yenawine, Hybrid Rocket Engines: Development of Composite Fuels with Complex 3D Printed Ports (Master's thesis), Dept. Mech. Aerosp. Eng., Coral Gables, FL, 2019.

[72] L. Galfetti, L. Merotto, M. Boiocchi, F. Maggi, L.T. De Luca, Ballistic and rheological characterization of paraffin-based fuels for hybrid rocket propulsion, in: 47th AIAA/ASME/SAE/ASEE Jt. Propuls. Conf. Exhib., 2011, pp. 1–17, http://dx.doi.org/10.2514/6.2011-5680.

[73] J. McCulley, A. Bath, S.A. Whitmore, Design and testing of FDM manufactured paraffin-ABS hybrid rocket motors, in: 48th AIAA/ASME/SAE/ASEE Jt. Propuls. Conf. Exhib., 2012, pp. 1–24, http://dx.doi.org/10.2514/6.2012-3962.

[74] D. Armold, J.E. Boyer, K. Kuo, J.K. Fuller, J. Desain, T.J. Curtiss, Test of hybrid rocket fuel grains with swirl patterns fabricated using rapid prototyping technology, in: 49th AIAA/ASME/SAE/ASEE Jt. Propuls. Conf., San Jose, CA, 2013, pp. 1–14, http://dx.doi.org/10.2514/6.2013-4141.

[75] D.M. Armold, J.E. Boyer, B. McKnight, K. Kuo, J. Desain, B.B. Brady, J. Fuller, T.J. Curtiss, Testing of hybrid rocket fuel grains at elevated temperatures with swirl patterns fabricated using rapid prototyping technology, in: 50th AIAA/ASME/SAE/ASEE Jt. Propuls. Conf., Cleveland, OH, 2014, pp. 1–13, http://dx.doi.org/10.2514/6.2014-3754.

[76] C. Hill, C.C. McDougall, T. Messinger, C.T. Johansen, Modification of paraffin-based hybrid rocket fuels using structural lattices, in: AIAA Propul. Energy 2019 Forum, Indianapolis, IN, 2019, pp. 1–10, http://dx.doi.org/10.2514/6.2019-4191.

[77] C. Hill, C.T. Johansen, Evaluation of lattice-augmented hybrid rocket fuels on a slab burner, in: AIAA Propul. Energy 2021 Forum, Virtual Event, 2021, pp. 1–12, http://dx.doi.org/10.2514/6.2021-3518.

[78] D. Zdybal, W. Klos, P. Drozdz, Z. Rydz, K. Kobus, B. Wyciszkiewicz, A. Zwolak, M. Wyzlinski, T. Tatara, A. Guzik, Performance of solid state emulsions of isoamyl alcohol in EVA-stabilized low-MW polyethylene, structured by laser-sintered nylon scaffolds as fuels in N2O hybrid rocket engine, in: AIAA Propul. Energy 2019 Forum, Indianapolis, IN, 2019, pp. 1–19, http://dx.doi.org/10.2514/6.2019-4335.

[79] D. Zdybal, L. Pabarcius, A. Laczewski, B. Wyciszkiewicz, A. Zwolak, P. Slawecki, M. Wyzlinski, Investigation of FDM-printed open-framework-reinforced helical PEWAX grains as a robust, high regression hybrid rocket fuel, in: AIAA Scitech 2021 Forum, Virtual Event, 2019, p. 1247, http://dx.doi.org/10.2514/6.2021-1247.

[80] Z. Wang, X. Lin, F. Li, X. Yu, Combustion performance of a novel hybrid rocket fuel grain with a nested helical structure, Aerosp. Sci. Technol. 97 (2020) 105613, http://dx.doi.org/10.1016/j.ast.2019.105613.

[81] Sasol website, products and applications, microcrystalline waxes, 2021, https://www.sasolwax.com/fileadmin/sasolwax/Personal_Care_Waxes_and_Petroleum_jellies.pdf, Accessed: 2021-09.

[82] Merck Website, Polystyrene-block-poly(ethylene-ran-butylene)-block-polystyrene-graft-maleic Anhydride, 2021, https://www.sigmaaldrich.com/catalog/product/aldrich/432431?lang=it&region=IT, Accessed: 2021-09.

[83] Prusa website, filament PLA, 2021, https://shop.prusa3d.com/fotky/PLA_TechSheet_ENG.pdf, Accessed: 2021-09.

[84] Prusa website, filament ASA/ABS, 2021, https://shop.prusa3d.com/en/filament/134-orange-easyabs-filament-1kg.html, Accessed: 2021-10.

[85] Filoalfa website, 2021, https://www.filoalfa3d.com/gb/content/15-nylon, Accessed: 2021-09.

[86] Prusa website, 2021, https://www.prusa3d.it/, Accessed: 2021-05.

[87] Prusa website, PrusaSlicer, 2022, https://www.prusa3d.it/prusaslicer/, Accessed: 2022-02.

[88] Stratasys website, materials, nylon 6, 2020, https://www.stratasys.com/materials/search/fdm-nylon-6, Accessed: 2020-06.

[89] Phantom 710 data sheet, 2020, https://www.adept.net.au/cameras/visionresearch/pdf/PhantomV710.pdf, Accessed: 2020-08.

[90] MATLAB website, Image Processing Toolbox, 2021, https://www.mathworks.com/products/image.html, Accessed: 2021-08.

[91] MATLAB website, Image Processing Toolbox, imadjust command, 2021, https://it.mathworks.com/help/images/ref/imadjust.html, Accessed: 2021-08.

[92] MATLAB website, image processing toolbox, drawcircle command, 2021, https://it.mathworks.com/help/images/ref/drawcircle.html?searchHighlight=drawcircle&s_tid=srchtitle_drawcircle_1, Accessed: 2021-08.

[93] S.A. Whitmore, S. Merkley, Radiation heating effects on oxidizer-to-fuel ratio of additively manufactured hybrid rocket fuels, J. Propul. Power 35 (4) (2019) 863–878, http://dx.doi.org/10.2514/1.B37037.

[94] H. Schlichting, Boundary-Layer Theory, McGraw-Hill Book Company, New Yoirk, NY, USA, 1979.

[95] L.F. Moody, Friction factors for pipe flow, Trans. Asme 66 (1944) 671–684.

[96] S. Kilic, M.A. Karabeyoglu, J. Stevens, B.J. Cantwell, Modeling the slump characteristics of the hydrocarbon-based hybrid rocket fuels, in: 39th AIAA/ASME/SAE/ASEE Jt. Propuls. Conf. Exhib., 2003, pp. 1–22, http://dx.doi.org/10.2514/6.2003-4461.

[97] F. Piscitelli, G. Saccone, A. Gianvito, G. Cosentino, L. Mazzola, Characterization and manufacturing of a paraffin wax as fuel for hybrid rockets, Propuls. Power Res. 7 (3) (2018) 218–230, http://dx.doi.org/10.1016/j.jppr.2018.07.007.